Nucleon Decay Searches with large Liquid Argon TPC Detectors at Shallow Depths: atmospheric neutrinos and cosmogenic backgrounds

A. Bueno,[1] Z. Dai,[2] Y. Ge,[2] M. Laffranchi,[2] A.J. Melgarejo,[1] A. Meregaglia,[2] S. Navas,[1] and A. Rubbia[2]

[1] *Dpto de Física Teórica y del Cosmos & C.A.F.P.E., Universidad de Granada, Granada, Spain*
[2] *Institute for Particle Physics, ETH Hönggerberg, Zürich, Switzerland*

(Dated: January 13, 2007)

Grand Unification of the strong, weak and electromagnetic interactions into a single unified gauge group is an extremely appealing idea which has been vigorously pursued theoretically and experimentally for many years. The detection of proton or bound-neutron decays would represent its most direct experimental evidence. In this context, we studied the physics potentialities of very large underground Liquid Argon Time Projection Chambers (LAr TPC). We carried out a detailed simulation of signal efficiency and background sources, including atmospheric neutrinos and cosmogenic backgrounds. We point out that a liquid Argon TPC, offering good granularity and energy resolution, low particle detection threshold, and excellent background discrimination, should yield very good signal over background ratios in many possible decay modes, allowing to reach partial lifetime sensitivities in the range of $10^{34} - 10^{35}$ years with exposures up to 1000 kton×year, often in quasi-background-free conditions optimal for discoveries at the few events level, corresponding to atmospheric neutrino background rejections of the order of 10^5. Multi-prong decay modes like e.g. $p \to \mu^- \pi^+ K^+$ or $p \to e^+ \pi^+ \pi^-$ and channels involving kaons like e.g. $p \to K^+ \bar{\nu}$, $p \to e^+ K^0$ and $p \to \mu^+ K^0$ are particularly suitable, since liquid Argon imaging provides typically an order of magnitude improvement in efficiencies for similar or better background conditions compared to Water Cerenkov detectors. Up to a factor 2 improvement in efficiency is expected for modes like $p \to e^+ \gamma$ and $p \to \mu^+ \gamma$ thanks to the clean photon identification and separation from π^0. Channels like $p \to e^+ \pi^0$ or $p \to \mu^+ \pi^0$, dominated by intrinsic nuclear effects, yield similar efficiencies and backgrounds as in Water Cerenkov detectors. Thanks to the self-shielding and 3D-imaging properties of the liquid Argon TPC, this result remains valid even at shallow depths where cosmogenic background sources are important. We consider the possibility of a very large area annular active muon veto shield in order to further suppress cosmogenic backgrounds at shallow depths. In conclusion, we find that this class of detectors does not necessarily require very deep underground laboratories, like those typically encountered in existing or planned sites, to perform very sensitive nucleon decay searches. In addition to a successful completion of the required R&D necessary to reach a relevant liquid Argon mass scale of 100 kton in a cost-effective way, we finally stress the importance of an experimental verification of the liquid Argon TPC physics potentialities to detect, reconstruct and classify events in the relevant GeV energy range. This experimental verification will require in addition to possible specific tests in charged particle beams, the collection of neutrino event samples with statistics in the range of 100'000 events or more, accessible e.g. with a medium-sized detector at near sites of long baseline artificial neutrino beams.

PACS numbers: 13.30.-a, 14.20.Dh, 29.40.Gx

I. INTRODUCTION

Grand Unification (GU) of the strong, weak and electromagnetic interactions into a single unified gauge [1, 2] is an extremely appealing solution which has been vigorously pursued, theoretically and experimentally, for many years. An experimental hint in its favor is the apparent merging of the three coupling constants at a large energy scale ($\sim 10^{16}$ GeV) when low energy measurements are extrapolated [3]. On the other hand, the most convincing experimental evidence for GU would be the direct observation of baryon number violation [4]. The experimental search for decays of protons or bound-neutrons is therefore one of the most important and unsolved problem of particle physics.

In the simplest Grand Unified Theories (GUT), nucleon decay proceeds via an exchange of a massive boson X between two quarks in a proton or in a bound neutron. In this reaction, one quark transforms into a lepton and another into an anti-quark which binds with a spectator quark creating a meson. According to the experimental results from Super-Kamiokande [5, 6] constraining the partial decay to $\tau/B(p \to e^+\pi^0) > 5.4 \times 10^{33}$ years (90%C.L.), the minimal SU(5) [2], predicting a proton lifetime proportional to $\alpha^{-2} M_X^4$ where α is the unified coupling constant and M_X the mass of the gauge boson X, seems definitely ruled out.

Supersymmetry, motivated by the so-called "hierarchy problem", postulates that for every SM particle, there is a corresponding "superpartner" with spin differing by 1/2 unit from the SM particle [7]. In this case, the unification scale turns out higher, and pushes up the proton lifetime in the $p \to e^+\pi^0$ channel up to $10^{36\pm1}$ years, compatible with experimental results. At the same time, alternative decay channels open up via dimension-five operator interactions with the exchange of heavy supersymmetric particles. In these models, transitions from one quark

family in the initial state to the same family in the final state are suppressed. Since the only second or third generation quark which is kinematically allowed is the strange quark, an anti-strange quark typically appears in the final state for these interactions. The anti-strange quark binds with a spectator quark to form a K meson in the final state [8]. The searches for decays $p \to \bar{\nu}K^+$, $n \to \bar{\nu}K^0$, $p \to \mu^+K^0$ and $p \to e^+K^0$ modes were also performed in Super-Kamiokande [9, 10] yielding counts compatible with background expectations, leading to limits on possible minimal SUSY SU(5) models [11, 12, 13]. The theoretical predictions, however, vary widely, since there are many new unknown parameters introduced in these models.

Other alternative models have been discussed in the litterature [14, 15, 16, 17, 18, 19, 20, 21, 22, 23, 24, 25, 26] (see Table I). In addition to the above mentioned GUTs, other supersymmetric SUSY-GUT, SUGRA unified models, unification based on extra dimensions, and string-M-theory models are also possible (see Ref. [27] for a recent review). All these models predict nucleon instability at some level. Finally, it is also worth noting that theories without low-energy super-symmetry [23, 28] predict nucleon decay lifetimes in the range $10^{35\pm1}$ years.

Some experimental aspects of nucleon decay detection were discussed in Ref. [29]. Nucleon decay signals are characterized by (a) their topology and (b) their kinematics. The presence of a lepton (electron, muon or neutrino) in the final state is expected, and in general few other particles (two body decays are kinematically favored), and no other energetic nucleon. The total energy of the event should be close to the nucleon mass and the total momentum should be balanced, with the exception of the smearing introduced by Fermi motion and other nuclear effects (nuclear potential, re-scattering, absorption, etc.) for bound decaying nucleons.

The search for nucleon decay therefore requires (1) excellent tracking and calorimetric resolutions to constrain the final state kinematics and suppress atmospheric neutrino backgrounds, (2) particle identification (in particular kaon tagging) for branching mode identification (3) very massive detectors and (4) underground locations to shield against cosmic-ray induced backgrounds, although the exact required rock overburden depends on the chosen detection technology. Fine tracking in the low momentum range (∼100–1000 MeV/c) is fundamental for (dE/dx) measurement, particle identification and vertex reconstruction.

In order to significantly improve current experimental results, next generation massive underground detectors satisfying the above requirements have to be considered. Given the variety of predicted decay modes open by the new theories, the ideal detectors should be as versatile as possible, very good in background rejection, and at the same time have the largest possible mass. The relevant factor is in fact M×ϵ, where M is the detector mass and ϵ the signal detection efficiency after cuts to suppress backgrounds, which depends on the considered decay channel. Hence large masses must be coupled to fine tracking and excellent calorimetry, to suppress atmospheric neutrino and cosmogenic backgrounds with a good signal selection efficiency. Furthermore, the detector should be sensitive to several different channels in order to better understand the nucleon decay mechanism. Since there are about 6×10^{32} nucleons per kton of mass, the proton lifetime limit (90% CL) in case of absence of signal and backgrounds is about $\tau_p/\mathrm{B} > \mathrm{M\ (kton)} \times \epsilon \times \mathrm{T} \times 10^{32}$ years, where T is the exposure in years and B the assumed branching fraction for the searched mode. Therefore, the required effective mass M×ϵ to reach 10^{35} years is in the range of 100 kton assuming T=10 years.

Such massive underground detectors will be sort of observatories for rare physics phenomena like astrophysical neutrino detection and nucleon decay searches, with possible synergies with existing or new artificial neutrino beams for improved understanding of neutrino flavor oscillations, including the possible identification of direct CP-violation in the leptonic sector (see e.g. Ref. [30] and references therein).

Among the various options and technologies currently thought of (see Ref. [31] and Refs. [32, 33, 34, 35, 36, 37, 38]), the Liquid Argon Time Projection Chamber [39, 40, 41, 42, 43, 44, 45, 46, 47, 48] (LAr TPC) is a powerful detector for uniform and high accuracy imaging of massive active volumes. It is based on the fact that in highly pure Argon, ionization tracks can be drifted over distances of the order of meters. Imaging is provided by position-segmented electrodes at the end of the drift path, continuously recording the signals induced. T_0 is provided by the prompt scintillation light.

Early work on the detection of nucleon decays in liquid Argon can be found in Ref. [49]. The liquid Argon TPC is a very promising detector option which satisfies at best the above mentioned requisites in terms of granularity, energy resolution and imaging capabilities if it can be extrapolated to the relevant mass scale.

In this paper we study the performance of a very massive Liquid Argon TPC as a nucleon decay detector. In the present study, we address for the first time the effect of the charged cosmic rays background as a function of the depth (i.e. rock overburden) of the underground detectors. In particular, we address the possibility to perform proton decay searches in "shallow depth" configurations [31]. Since the new large underground detectors will require either a new site to be excavated or the extension of an existing infrastructure, it is important to understand if very-sensitive nucleon decay searches do necessarily require deep underground locations, like those typically encountered in existing or planned laboratories [50].

The paper is organized as follows: some considerations about the conceptual design of the detector are outlined in section II. The discussion of the assumed detector configuration and the simulated physics process for signal and background events are described in section III. The description of the analysis cuts designed to suppress at-

Model	Ref.	Modes	τ_N (years)
Minimal $SU(5)$	Georgi, Glashow [2]	$p \to e^+\pi^0$	$10^{30} - 10^{31}$
Minimal SUSY $SU(5)$	Dimopoulos, Georgi [11], Sakai [12] Lifetime Calculations: Hisano, Murayama, Yanagida [13]	$p \to \bar{\nu}K^+$ $n \to \bar{\nu}K^0$	$10^{28} - 10^{32}$
SUGRA $SU(5)$	Nath, Arnowitt [14, 15]	$p \to \bar{\nu}K^+$	$10^{32} - 10^{34}$
SUSY $SO(10)$ with anomalous flavor $U(1)$	Shafi, Tavartkiladze [16]	$p \to \bar{\nu}K^+$ $n \to \bar{\nu}K^0$ $p \to \mu^+K^0$	$10^{32} - 10^{35}$
SUSY $SO(10)$ MSSM (std. $d = 5$)	Lucas, Raby [17], Pati [18]	$p \to \bar{\nu}K^+$	$10^{33} - 10^{34}$
		$n \to \bar{\nu}K^0$	$10^{32} - 10^{33}$
SUSY $SO(10)$ ESSM (std. $d = 5$)	Pati [18]	$p \to \bar{\nu}K^+$	$10^{33} - 10^{34}$ $\lesssim 10^{35}$
SUSY $SO(10)/G(224)$ MSSM or ESSM (new $d = 5$)	Babu, Pati, Wilczek [19, 20, 21], Pati [18]	$p \to \bar{\nu}K^+$	$\lesssim 2 \cdot 10^{34}$
		$p \to \mu^+K^0$	$B \sim (1 - 50)\%$
SUSY $SU(5)$ or $SO(10)$ MSSM ($d = 6$)	Pati [18]	$p \to e^+\pi^0$	$\sim 10^{34.9\pm1}$
Flipped $SU(5)$ in CMSSM	Ellis, Nanopoulos and Wlaker[22]	$p \to e/\mu^+\pi^0$	$10^{35} - 10^{36}$
Split $SU(5)$ SUSY	Arkani-Hamed, *et. al.* [23]	$p \to e^+\pi^0$	$10^{35} - 10^{37}$
$SU(5)$ in 5 dimensions	Hebecker, March-Russell[24]	$p \to \mu^+K^0$ $p \to e^+\pi^0$	$10^{34} - 10^{35}$
$SU(5)$ in 5 dimensions option II	Alciati *et.al.*[25]	$p \to \bar{\nu}K^+$	$10^{36} - 10^{39}$
GUT-like models from Type IIA string with D6-branes	Klebanov, Witten[26]	$p \to e^+\pi^0$	$\sim 10^{36}$

TABLE I: Summary of the expected nucleon lifetime in different theoretical models.

mospheric neutrino and muon-induced backgrounds from proton and neutron decay channels are given in section IV. Finally, the results obtained in terms of lifetime sensitivities for the considered decay modes are given in section V.

II. DETECTOR CONCEPT

Our analysis assumes the scalable concept of a liquid Argon TPC, as proposed in [51] (see Figure 1). Other designs have been presented in Ref. [52]. An LOI based on a more standard configuration and a surface detector has also been submitted to FNAL [53].

The design of Ref. [51] relies on (a) industrial tankers developed by the petrochemical industry (no R&D required, readily available, safe) and their extrapolation to underground or shallow depth LAr storage, (b) novel readout methods with embedded charge chain for very long drift paths, based on e.g. LEM readout, (c) new solutions for very high drift voltage, (d) a modularity at the level of 100 kton and (e) the possibility to embed the LAr in a magnetic field [54]. Such a scalable, single LAr tanker design is the most attractive solution from the point of view of physics, detector construction, operation and cryogenics, and finally cost.

An R&D program is underway with the aim of optimizing the design [55]. Concerning the further consolidation of the technology, we point out that a test-beam dedicated to the reconstruction and separation of electrons from neutral pions has been discussed [56]. In addition, a $\simeq 100$ ton liquid Argon TPC to complement the 1 kton Water Cerenkov detector at the potential 2 km site 2.5^o off-axis from the T2K beam has also been considered [57]. If realized, this unique experimental setup will allow to compare the performance of the liquid Argon TPC to the Water Cerenkov ring imaging and to reconstruct neutrino events directly in the same beam with a statistics of more than 100'000 events per year, sufficient to extrapolate the atmospheric neutrino background in a potential 1000 kton×year exposure. ICARUS T600 [44], to be commissioned in the coming years, will detect too few contained events to demonstrate the ultimate physics performance of the technology.

When operating TPCs with long drift paths and charge amplification at the anode as the one considered here, one must pay attention to possible drift field distortions caused by the space charge created by the positive ions slowly drifting towards the cathode. Indeed, it is well known that ion (and hole) mobility in liquid

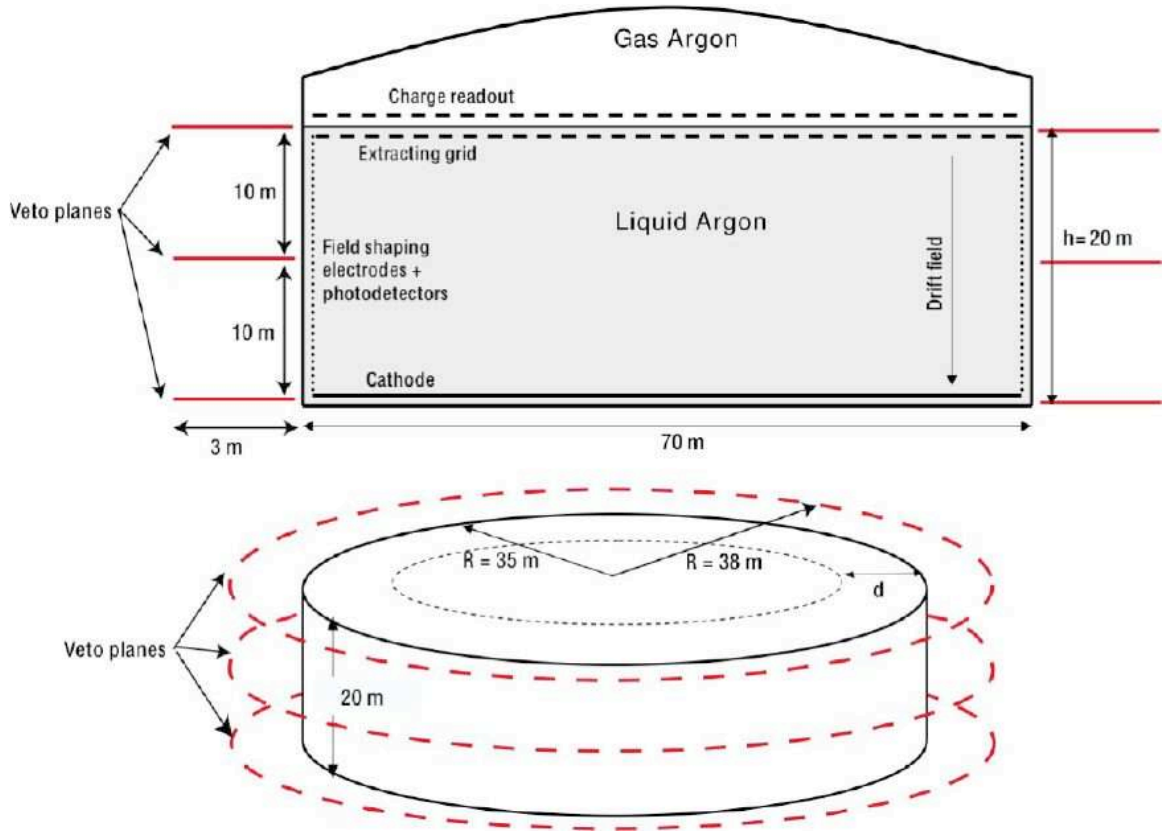

FIG. 1: Conceptual design of a 100 kton LAr TPC detector (see Ref. [51] for details). To suppress cosmogenic backgrounds, we consider the possibility to locate three large area veto planes to detect remaining penetrating cosmic ray muons passing in the vicinity of the Argon detector (see text).

Argon is small compared to that of electrons ($\mu_{ions} \approx (10^{-2} \div 10^{-3})\mu_e$), and inconsistencies among experimental measurements were attributed to the influence of the motion of the liquid itself [58].

The problem of ions accumulating in the TPC drift volume has been effectively overcome by introducing an additional grid ('gate') between the drift volume and the readout plane [59, 60]. The gate is normally closed and only opens for a short period of time when an external trigger signals an interesting event. This method is easily applicable to our design in the case of a pulsed artificial neutrino beam source, as the one considered in Ref. [30].

In the case of proton decay (or atmospheric neutrino background) where the detector must be continuously sensitive, the prompt scintillation light with an appropriate detection threshold (e.g. > 100 MeV) could be used to signal the (rare) occurrence of interesting events. Unfortunately, this is impracticable at shallow depths because, as it will be shown later, the fiducial volume occupancy is dominated by remaining cosmic ray events crossing the detector: at a rock overburden $\lesssim 1$ km w.e., the average number of cosmic ray muons crossing the detector within a drift time is $\gtrsim 1$ (see Table III). This situation worsens when the rock overburden is decreased.

Hence, either the rock-overbuden is $\gtrsim 1$ km w.e. or the TPC must be continuously active and we must consider space charge effects from accumulating ions in the liquid Argon volume. It is possible to show that asymptotically the stationary density of ions ρ_i in the drift volume of a double phase readout system with charge amplification is given by:

$$\rho_i(t \to \infty) \simeq \frac{G\epsilon_{feedback}\eta_{v-l}\epsilon_{grid}\left\langle \frac{dE}{dx} \right\rangle x}{\mu_{ions} E W_e(E)} \phi_\mu \qquad (1)$$

where G is the average gain of the charge readout system, $\epsilon_{feedback}$ is the efficiency for ions to feed-back into the gas region below the charge amplification planes, η_{v-l} is the efficiency for ions to be transmitted from the gaseous phase into the liquid phase, ϵ_{grid} is the transparency of the extraction grid when traveling from the higher extraction field to the lower drift field, $< dE/dx >$ is the average stopping power of the cosmic ray muons, x is the average path of the muons in the fiducial volume, ϕ_μ the flux of cosmic muons at the detector upper surface per unit surface and per unit time, μ_{ions} is the ion mobility, E the electric drift field and $W_e(E)$ the field-dependent average energy expended by a cosmic ray muon to create an ion-electron pair in the medium (field dependence arises from columnar ion-electron recombination [46]).

Assuming a stationary situation, ionization electrons

will drift in a medium homogeneously filled with the above calculated density of ions. The resulting free electron lifetime can be estimated as $\tau_e = 1/\left(k_r(E)\rho_i\right)$ where k_r is the electron-ion recombination rate (which depends on the electric field).

We note that $\epsilon_{feedback} \ll 1$, because of electron diffusion in the amplification gap, as a result of which ions can follow field lines ending up on the electrodes of the amplification system rather than on the external field lines; this is particularly true for the devices with multiple stages that we operate [61]. In addition, $\epsilon_{grid} \lesssim 0.3$ since the extraction field is typ. 3 kV/cm and the drift field is typ. 1 kV/cm.

The efficiency η_{v-l} for the transfer of positive ions from the vapour into the liquid Argon phase has, as far as we know, not being measured. When the distance between the ion and the liquid-vapor interface is greater than several Angstroms (the Argon bond length is ≈ 3.7 $\mathring{A}$), the liquid may be treated as a continuum [62]. Assuming a planar interface between the liquid and vapor, the situation is then comparable to a boundary-value problem with dielectrics and can be solved with the charge-image method in a single dimension: a point charge q in the medium ϵ at the interface with a medium ϵ' feels a charge image q' in the medium ϵ' given by $q' = -(\epsilon'-\epsilon)/(\epsilon'+\epsilon)q$. For $\epsilon' > \epsilon$, $q.q' < 0$ and the force is attractive. For $\epsilon' < \epsilon$, $q.q' > 0$ and the force is repulsive. Given the difference in dielectric constants between the liquid Argon $\epsilon_l \simeq 1.54$ and its gas phase $\epsilon_v \simeq 1$, a charge in the liquid will feel a repulsive force from the interface, while a charge in the gas will be attracted to the interface and will tend to "stick" at the surface. The potential energy of the charge q placed at a distance $d > 0$ from the planar liquid-vapor interface is [62, 63, 64, 65]:

$$V_l(d) = \frac{q^2}{16\pi\epsilon_0\epsilon_l}\left(\frac{\epsilon_l - \epsilon_v}{\epsilon_l + \epsilon_v}\right)\frac{1}{d} \equiv \frac{A_l}{d} \tag{2}$$

$$V_v(d) = \frac{q^2}{16\pi\epsilon_0\epsilon_v}\left(\frac{\epsilon_v - \epsilon_l}{\epsilon_l + \epsilon_v}\right)\frac{1}{d} \equiv \frac{A_v}{d} \tag{3}$$

where the index corresponds to the charge in the liquid (l) or in the vapor (v). Classically, the potential barrier is infinite at the interface ($d = 0$) and a quantum mechanical treatment is needed. In practice, one can also assume that in order to cross the boundary the charge must pass above a finite, classical potential, whose height is to be determined experimentally [63].

In the presence of an external difference of potential to create a drift field, the total potential energy is $V(x) = V_l(|x|) + qE_l x$ for $x < 0$ (liquid phase) and $V(x) = V_v(x) + qE_v x$ for $x \geq 0$ (vapor phase), where E_l (resp. $E_v = (\epsilon_l/\epsilon_v)E_l$) is the induced electric field in the liquid (resp. vapor) phase.

Experimental data has been collected on the extraction of quasi-free electrons from liquid into gaseous Argon [65]. The potential felt by such electrons is illustrated in Figure 2. It is plotted in units of kT where $T = 87$ K is the temperature of the liquid Argon at normal pressure. Photoelectric effect measurements indicate

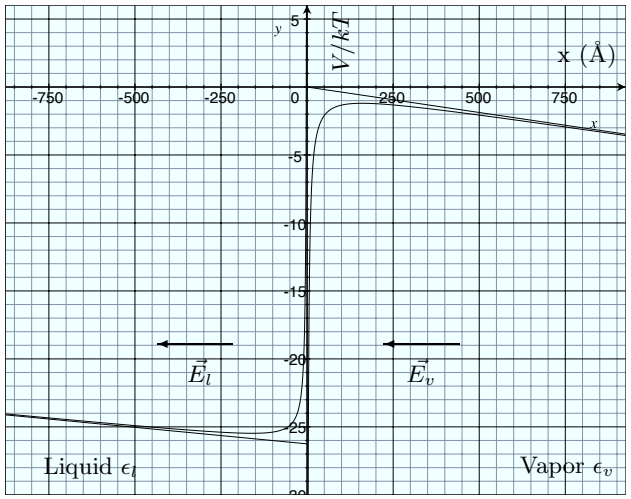

FIG. 2: Illustration of the potential felt by quasi-free electrons as a function of the position x in $\mathring{A}$ across the liquid-vapor interface in the presence of an external drift field. The potential is given in units of kT where $T = 87$ K is the temperature of the liquid Argon at normal pressure.

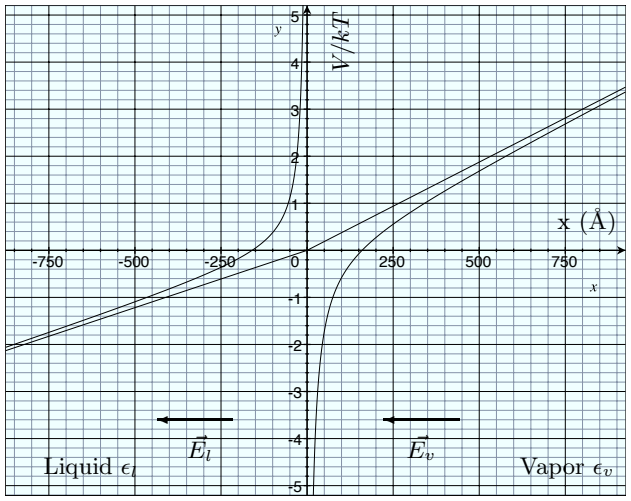

FIG. 3: Same as Figure 2 but for positive ions.

that the electrons in the liquid are shifted by an amount $V_0 = -0.21$ eV with respect to the energy in vacuum (or vapor) [66]. The external drift field and the repulsive potential at the interface generate a minimum potential in the liquid phase at a distance $d_m^l = (A_l/eE_l)^{1/2}$ from the interface with a value $V_m^l = 2(A_l e E_l)^{1/2}$ and similarly in the gas phase. The barrier height as seen from the minimum in the liquid at $x = -d_m$ is therefore $\Delta V(E) = V_0 - V_m^l - V_m^v = V_0 - 2e^{1/2}\left(A_l^{1/2}E_l^{1/2} + A_v^{1/2}E_v^{1/2}\right)$. The mean life time to traverse the interface (or trapping time) can be analyzed with the aid of the Smoluchowski equation [63], predicting $\tau_e \propto \exp(\Delta V/kT)$. Experi-

mental data however indicate that the above-calculated thermionic current is increased by a rate $\propto \mu E/\lambda_1$ where λ_1 is the momentum-transfer mean free path, as predicted by the Shottky model of electric field enhanced thermionic emission [65], giving $\tau_e \propto \exp(\Delta V/kT)/E$, with a stronger influence of the drift field.

In the case of the ions, the potential for a positive charge is illustrated in Figure 3. The ion is attracted very near the interface and must tunnel through the repulsive potential existing on the liquid side of the interface in order to enter the liquid. A semi-classical approach is not justified. The transport of Tl positive ions from xenon vapor to liquid was successfully reported with a $\simeq 10\%$ efficiency in Ref. [67]. There appears to be a difference in the behavior of positive ions between the liquid-to-gas and gas-to-liquid transition [62]. While electrons could traverse the liquid-vapor interface the positive ions could not. This is consistent with the fact that the ion mobility in the liquid is too small to allow for the external field to enhance the thermionic emission. However, the transmission of negative ions through the liquid-vapor interface of neon has been observed with trapping time of the order of 10–100 s at fields of 0.1–1 kV/cm [64]. This is explained by the type of clustering around the different species of particles. If a sort of bubble surrounds negative charges then the breaking of the bubble at the surface could let them escape. In conclusion, the phenomenon of transfer of the ions through the interface is expected to be rather complicated, not well understood and has not been measured. In the case relevant to this paper, it is likely that some fraction of the Argon ions will cross into the liquid, although possibly with long trapping times, and experimental studies are needed to assess how much. For safety, we will conservatively assume full transmission of Argon ions across the interface.

We note that competing with the process of transfer from the gas to liquid is the radial drifting of ions at the surface of the liquid-gas interface towards the edges of the volume, until they reach the field shaping electrodes. There they are neutralized by the external power supply.

We now compute the free electron lifetime due to the recombination with the accumulating ions. In the *worst case* considered in this paper corresponding to the "under the hill location" (see Table III), we contemplate $\simeq 1000$ muons crossing the detector per second. We conservatively assume that each of these muons will vertically cross the entire drift region, hence $x \simeq h = 20$ m, that the average charge gain is $G \simeq 150$ (see Ref. [51]), very conservatively that $\epsilon_{feedback} \simeq 0.5$, $\eta_{v-l} \simeq 1$ although we expect this to be a pessimistic assumption, $\epsilon_{grid} \simeq 0.3$ and that the ion mobility in the range $(0.2 \div 1) \times 10^{-3}$ cm^2/V/s [58]. These assumptions yield $\rho_i \simeq (0.7 \div 3.7) \times 10^5$ ions/cm^3. Assuming a recombination rate $k_r = 1 \times 10^{-4}$ cm^3/s, consistent with measurements at the relevant electric drift fields [68], implies that the electron lifetime due to ion accumulation in the medium is $\tau_e > 30 \div 140$ ms, to be compared with a maximum electron drift time ~ 10 ms. We stress that actual values of $\epsilon_{feedback}$ and η_{v-l} are expected to increase these values even further. We conclude that in all configurations considered in this paper, charge attenuation due to recombination with ions in the medium is expected to be negligible compared to other charge attenuating effects, like e.g. attachment to electronegative impurities in the Argon [45].

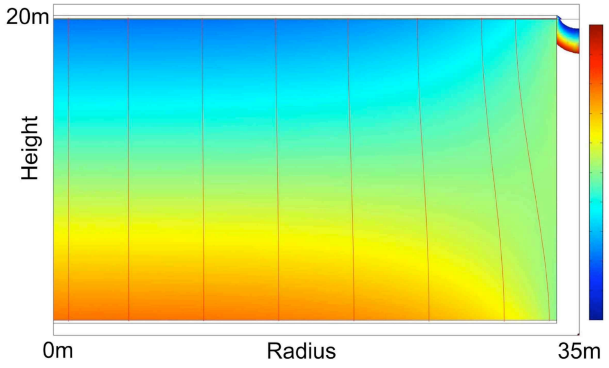

FIG. 4: Drift field map with an unrealistic ion charge density of 2×10^5 ions/cm^3=4×10^{-8} C/m^3 (see text). The field distortion is $\pm 30\%$. Dark blue corresponds to 0.5 kV/cm and red to 1.5 kV/cm.

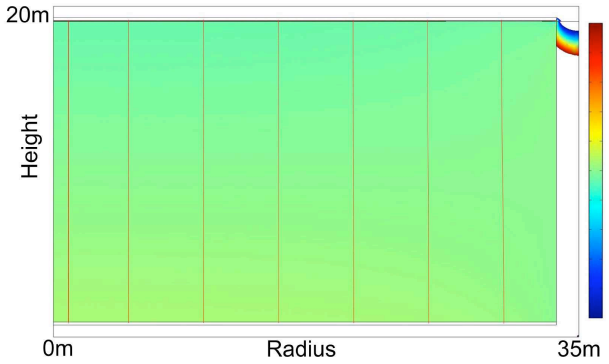

FIG. 5: Same as Figure 4 with a ion charge density of 2×10^4 ions/cm^3=4×10^{-9} C/m^3. The field distortion is $\pm 3\%$.

We now turn to the drift field map distortions. The results of numerical simulations for the electric field assuming a homogeneous positive charge density distribution in the liquid Argon fiducial volume of resp. $\rho_i = 2 \times 10^5$ ions/cm^3 and 2×10^4 ions/cm^3 and the contributions of ions directly produced in the ionization process are shown in resp. Figures 4 and 5. The cathode is placed at -2 MV and the volume is enclosed by field shaping electrodes. Dark blue corresponds to 0.5 kV/cm and red to 1.5 kV/cm. With an unrealistic ion charge density of 2×10^5 ions/cm^3=4×10^{-8} C/m^3, the field is distorted by $\pm 30\%$. As expected, for a more realistic charge density of 2×10^4 ions/cm^3, field variations are $\pm 3\%$. The effect of ions directly produced in the ionization is negligible.

We point out in this context that the realization and

successful operation on surface of a 5 m long detector column [55] (ARGONTUBE) will allow to experimentally verify these hypotheses and to prove the feasibility of detectors with long drift paths, hence representing a very important milestone in the conceptual proof of the detector design.

III. SIMULATION FRAMEWORK

As already pointed out in Section I, the nucleon decay searches aim at discoveries at the few event level in an atmospheric neutrino background sample of more than 10^5 events. The understanding of this background will require the collection of a commensurate sample in a neutrino beam of the relevant energy.

In the meantime, a reliable MC description of all physical effects involved is important to correctly estimate nucleon decay sensitivities. Whenever possible, our results are based on full simulations. Several neutron and proton decay channels with proper treatment of nuclear effects have been simulated. Likewise, the two dominant background sources relevant to our search were simulated in details: the atmospheric neutrino background and the cosmic muon-induced background. The next sections describe this in more details.

A. Detector geometry and simulation

We considered as reference detector a homogeneous volume of liquid Argon in a single giant volume composed of a cylindrical volume of 20 m height and 70 m diameter for a total of 100 kton. This geometry was implemented in a full simulation based on the `GEANT4` toolkit [69, 70].

For each event generated within the liquid Argon volume, final state particles are transported through the medium, with the possibility of secondary interactions. The detector effects have been included in the production and transport of the events by simulating the liquid Argon response. For ionizing particles, the deposited energies in microscopic sub-mm^3 volumes of Argon are used to compute the amount of ionization [46] and scintillation yields [71]. Ionization charge is collected in two perpendicularly segmented striped readout planes with 3 mm pitch. This information is digitized taking into account the response of a typical potential charge readout electronic preamplifier and is used to create the two perpendicular charge readout views. Scintillation light is propagated through the medium and collected on photodetectors located on the inner surface of the detector [96].

B. Nucleon decay signal simulation

Several neutron and proton decay channels have been studied (see Section IV). For each channel, 2000 signal events were generated and fully simulated inside the detector. Nucleon decay events are characterized by a definite value of the total energy and by the fact that the total momentum of the decay products must be zero. These features, which are true for the decay of a free nucleon, are only approximately verified for a nucleon bound in a nucleus.

The nuclear effects, the distortions of the energy and momentum distributions due to Fermi motion (since the recoil nucleus is not measured), and the reinteraction of decay particles with the nucleus have been treated with the `FLUKA` [72] package. The treatment is similar to that used for nuclear effects in neutrino interactions, see e.g. Ref. [73], and will be used also in the the context of simulation of atmospheric neutrino background (see Section III C).

In a given signal event, energy and relative orientation of the decay products are selected according to conservation laws and phase space. The resulting configuration is inserted into the target nucleus and used as initial step for the `PEANUT` [72] simulations. The position of the decaying nucleon in the nucleus is sampled from a probability distribution proportional to the density profile for the selected nucleon type. The Fermi motion of the original nucleon is then sampled according to the local Fermi distribution. The decay products are followed like any other secondary particle in `PEANUT`, thus exploiting all the details of its nuclear modeling, as described in the following paragraphs. See Ref. [72] and references therein for full details.

Nuclear effects in nucleon decays can be roughly divided into those of the nuclear potential and those due to reinteractions of decay products. Bound nucleons in nuclei are subject to a nuclear potential. The Fermi energy (or momentum) must be calculated from the bottom of this nuclear potential well, and the removal of a nucleon from any stable nucleus is always an endothermic reaction. When a nucleon decays, some energy is spent to take it out of this well: the minimum energy is given by the nucleon separation energy (around 8 MeV), and corresponds to the decay of a nucleon at the Fermi surface. In this case, the daughter nucleus is left on its ground state. More deeply bound nucleons decay leaving a hole in the Fermi sea, that corresponds to an excitation energy of the daughter nucleus, and an additional loss of energy of the decay products. This energy is then spent in evaporation and/or gamma deexcitation. Thus, the invariant mass of bound nucleon decay products is expected to be always slightly smaller than the free nucleon mass, and spread over a range of about 40 MeV. Correspondingly, the Fermi momentum of the decaying nucleon is transferred to the decay products and compensated by the recoil of the daughter nucleus. Additional momentum distortions come from the curvature of particle trajectories in the nuclear potential.

Reinteractions in the nuclear medium also play an important role. Decay products can lose part of their energy in collisions, or even be absorbed in the same nucleus where they have been created. This is particularly

true for pions, that have an important absorption cross section on nucleon pairs, while kaons have smaller interaction probability.

Nucleon-nucleon total cross sections, both elastic and inelastic, used in FLUKA are taken from available experimental data. Elastic scattering is explicitly performed according to the experimental differential cross sections. Pion induced reactions are more complex, mainly because of two- and three-nucleon absorption processes. Above the pion production threshold, the inelastic interactions are handled by the resonance model. Other pion-nucleon interactions proceed through the non-resonant channel and the p-wave channel with the formation of a Δ resonance, with modified resonance parameters taking into account nuclear effects.

The conservation of strangeness leads to very different interactions of the K^+, K^0 and K^-, $\bar{K}^0$ with nucleons at low energies. K^- have a large cross section for hyperon production, with the $\Sigma\pi$ and $\Lambda\pi$ channels always open. A detailed treatment of K^+ interactions has been developed in PEANUT, whereby the K^+ nucleon system is described by phase shift analysis. This treatment was used in the present analysis, where it was very relevant for the nucleon decays involving kaons. In particular, K^+ involved in proton decays are below 700 MeV/c, where the inelastic contributions are very small and elastic scattering does not affect strongly the efficiency. Charge exchange $K^+ + n \rightarrow K^0 + p$ can lead to a loss of efficiency. In the simulations of $p \rightarrow \bar{\nu}K^+$ decays, less than 4% of the kaons were lost due to nuclear processes (see Section IV). In comparison, in the simulated $p \rightarrow e^+\pi^0$ decays, the neutral pion is absorbed within the nucleus with a probability of $\simeq 50$ %.

In the treatment of nuclear reinteractions, the cross-sections are modified to avoid too short mean free paths in nuclear matter by taking into account Pauli blocking, antisymmetrization of fermions, hard-core effects and formation zone or coherence length for non-fragmenting processes. The intra-nuclear cascade step goes on until all nucleons are below 50 MeV and is followed by a pre-equilibrium emission phase in which additional nucleons can be emitted.

Many benchmarks showing good agreement between PEANUT results and nuclear reaction data can be found in the main Ref. [72].

C. Atmospheric neutrino background

The atmospheric neutrino flux has been computed by several groups. We take results from the FLUKA group [74] and the HKKM 2004 [75] (Honda) models. The FLUKA model is estimated to have a 7% uncertainty for the primary spectrum, 15% for the interaction model, 1% for the atmosphere profile, 2% for the geomagnetic field and a total 17% uncertainty. The HKKM model has about 10% uncertainty when the neutrino energy is below 10 GeV, but the uncertainties are still large when the neutrino energy is above 10 GeV, due to the uncertainties of the primary cosmic ray flux and the interaction model above 100 GeV.

The neutrino-cross sections and the generation of neutrino interactions are based on the NUX [76] code. This code can be used in fixed target mode for incoming neutrino energies from $\simeq$ 20 MeV up to 10 TeV. NUX can generate neutral current (NC) and charged current (CC) processes, and includes all basic processes to properly describe neutrino interactions in different kinematical regimes. In particular, a distinction is made among the following processes: quasi-elastic process (QE), inelastic process (DIS) [97] and charm production. These processes are appropriately matched to reproduce the total inclusive and existing exclusive experimental data to the best of current experimental knowledge. The mass of the outgoing lepton and of the target nucleon are taken into account in the kinematics and in the differential cross-section. In order to take into account nuclear effects, an interface with FLUKA was implemented, yielding the so-called NUX-FLUKA generator: a primary nucleon is chosen according to the density profile for the selected nucleon type and the Fermi motion of the original nucleon is sampled according to the local Fermi distribution, just as in the case of the nucleon decay simulation (see Section III B). A neutrino interaction is generated and the final state intra-nuclear cascade is taken into account by propagating final state particles through the nucleus with PEANUT.

The NUX-FLUKA model was benchmarked with the data of the NOMAD [77] experiment at high neutrino energies ($>$ 5 GeV), and was compared at low neutrino energies ($<$ 5 GeV) with other available generators like NUANCE [78] and was shown to give very similar particle multiplicities and distributions [79]. The production of strange particle at high energy was studied in NOMAD [80] and found to be properly described after tuning of the JETSET [81] fragmentation parameters. At low energy, the production of kaons primarily proceeds through the decay chain of baryon resonances. In this regime, the yield of kaon is very strongly suppressed compared to that of pions.

Table II reports the computed number of atmospheric neutrino events per neutrino flavor and per process type, normalized to an exposure of 1 kton$\times$year. In order to reach nucleon decay sensitivities in the range of 10^{35} years, exposures in the range of 1000 kton$\times$year will be considered. Therefore, the simulated data sets correspond to a total exposure of 1000 kton$\times$year or about 250'000 background events. Part of this atmospheric neutrino background sample was fully simulated and fully reconstructed. Typical atmospheric neutrino events in Argon viewed by two-dimensional charge readout planes with a pitch of 3 mm are shown in Figures 6 and 7. Full reconstruction of atmospheric neutrino events at low multiplicity is rather straight-forward. In particular, quasi-elastic events reconstruction is discussed in Ref. [82]. Actual performance on real quasi-elastic events

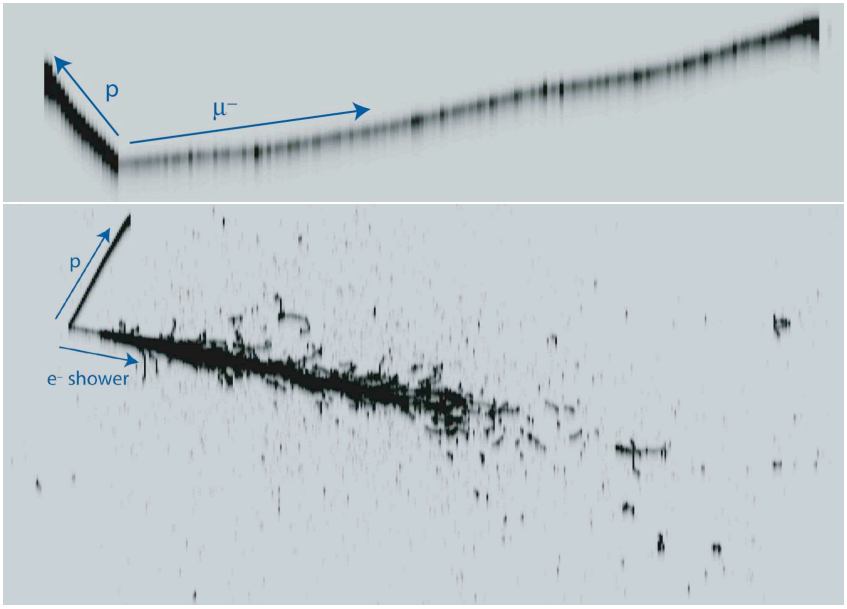

FIG. 6: Typical ν_μ and ν_e QE event in liquid Argon detector ($\nu_\mu + n \to p + \mu^-$ and $\nu_e + n \to p + e^-$).

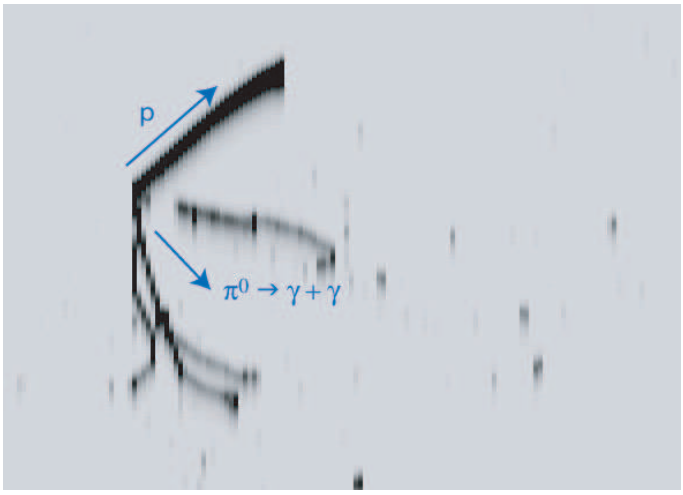

FIG. 7: Typical ν_μ NC event in liquid Argon detector ($\nu_\mu + p \to \nu_\mu + p + \pi^0$).

data can be found in Ref. [43]. See also Ref. [83] for a discussion of precision atmospheric neutrino measurements with a liquid Argon TPC.

In order to have the largest sample of events to estimate the backgrounds after selection cuts, a fast reconstruction program was developed which used Monte-Carlo tracks as input for pattern recognition. Energy and angular resolution of the detector were properly taken into account by means of the full simulation. On the other hand, particle reconstruction efficiency was introduced as momentum thresholds which depended on the particle type. These latter were approximately 5 MeV/c for electrons, 10 MeV/c for photons, 20 MeV/c for muons and pions, 30 MeV/c for kaons, and 300 MeV/c for protons. Checks were performed to ensure that the fast simulation reproduced the general features of the background events on the subsample of fully reconstructed events.

D. Cosmic muon-induced background

A second relevant source of background comes from particles produced by cosmic muons crossing and interacting in the liquid Argon volume, or muons avoiding the active liquid Argon but interacting in the vicinity of the detector. The main physical parameter determining the rate of this background is the rock overburden.

Atmospheric	ν_e CC (evts/kt/year)			$\bar{\nu}_e$ CC (evts/kt/year)		
Flux Model	DIS	QE	Tot	DIS	QE	Tot
FLUKA	22.9	49.0	71.9	7.2	8.4	15.6
($\bar{E}$(GeV))	(2.83)	(0.62)		(3.12)	(0.79)	
HKKM	22.7	45.6	68.3	7.2	7.8	15.0
($\bar{E}$(GeV))	(3.01)	(0.64)		(3.42)	(0.85)	
Atmospheric	ν_μ CC (evts/kt/year)			$\bar{\nu}_\mu$ CC (evts/kt/year)		
Flux Model	DIS	QE	Tot	DIS	QE	Tot
FLUKA	42.0	80.1	122.1	15.3	18.5	33.8
($\bar{E}$(GeV))	(4.53)	(0.72)		(4.89)	(0.90)	
HKKM	43.3	74.0	117.3	15.8	17.4	33.2
($\bar{E}$(GeV))	(4.78)	(0.77)		(5.19)	(0.98)	
Atmospheric	ν NC (inelastic)			$\bar{\nu}$ NC (inelastic)		
Flux Model	(evts/kt/year)			(evts/kt/year)		
FLUKA	23.2			9.0		
($\bar{E}$(GeV))	(3.73)			(4.08)		
HKKM	23.4			9.1		
($\bar{E}$(GeV))	(3.97)			(4.40)		

TABLE II: QE, DIS event rates per kton per year, and average energies for FLUKA 2002 and HKKM 2004 flux models and `NUX` neutrino cross-sections. In order to reach nucleon decay sensitivities in the range of 10^{35} years, exposure in the range of 1000 kton$\times$ year will be considered.

The cosmic muon intensity as a function of underground depth is obtained from Crouch's [84] fit to the world data and further updated by the Particle Data Group [85]. This parameterization agrees to better than 6% with the most recent MACRO measurements [86] at Gran Sasso. However, it cannot be applied to the case of a shallow depth detector. For this purpose, we generated cosmic μ^+'s and μ^-'s according to double differential distributions found in Ref. [85] on a large hemisphere at the surface of the Earth and transported them through rock. In the simulation, all physical processes were taken in account, including multiple scattering and energy losses.

We aimed at giving here the general trend and the magnitude of the background, while the precise determination of the muon induced background will depend on many site-specific features: (a) rock chemical composition, (b) exact distribution of rock overburden (c) detector configuration, cryostat, distance to rock, ...

Many relevant processes depend on rock chemical composition. For example, the neutron production per unit of rock mass depends on the average atomic number. The expected dependence according to Ref. [87] is $dN \propto A^{0.76}$, i.e., that means a difference of about 25% in neutron production going from standard rock ($\langle A \rangle = 22$) to the salt rock ($\langle A \rangle = 30$). Particle propagation through rock of secondary particles produced in muon interactions is also influenced by chemical composition, in first approximation with the same behaviour as the nuclear interaction length.

The angular distribution of muons underground depends on the actual distribution of rock overburden. If the Earth surface above the site is approximately flat, the muon intensity at an angle θ is given by the vertical intensity calculated at a depth $h' = h/\cos\theta$ multiplied by a factor $1/\cos\theta$ from the production probability in the atmosphere [84]. If, however, the detector is located in a mountain or under a hill, the muon intensity is determined by the actual rock overburden along any given direction. The most important effect is a different total muon intensity with respect to the flat surface case, and a secondary effect is the difference in veto efficiency (see Section III E) due to the different muon directionality. Indeed, the deeper the rock overburden, the more vertical the surviving muons.

Since, as we will show in the following paragraphs, secondary particles that enter the detector are produced in the first one or two meters of material around it, the actual material distribution/composition of the LAr container may affect the background and the veto conditions. This effect has been neglected at this stage and we have assumed rock composition around the fiducial liquid Argon volume.

We have considered different underground depths and two different geometries (see Tables III and IV) in order to explore possibilities at shallow depths: (a) under flat ground cover (e.g. a green-field site [98] or a mine with vertical access) at resp. approximately 3, 2, 1, 0.5, 0.13 km water equivalent, corresponding to resp. 1130 m, 755 m, 377 m, 188 m and 50 m of standard rock; and (b) detector under a hill configuration at shallow depth (see Figure 8). A green-field site, or a shallow-depth site under the hill were considered in the context of a synergy with an upgraded CNGS accelerator neutrino physics program [30].

The simulations of muon-induced background were performed using `FLUKA` and `GEANT4` toolkit and the results were compared. They were carried out in three steps: (1) in the first step we estimated the number of remaining cosmic muons crossing the detector or its vicinity per given unit time as a function of the detector's depth or its geographical configuration; (2) then we obtained particle fluxes at the detector surface from interactions of those cosmic ray muons in the surrounding rock as a function of the detector's depth; (3) the resulting neutron, kaon and lambda differential flux spectra, rescaled to the rate expected at a given depth, have then been used to simulate particle interactions inside the detector.

As far as `FLUKA` simulations are concerned, the cross section of the photo-nuclear interaction of high-energy muons is taken from Ref. [88] and validation of the `FLUKA` models for muon transport and muon photo-nuclear interactions can be found in Refs. [87, 89].

In the case of the detector under the hill, the topology of an existing location was studied [99] and a simple but conservative description of the rock profile was implemented in a `GEANT4` simulation. The parameters of the geometry in a 3D image from the `GEANT4` simulation

Depth		Code	All muons		$E_\mu > 1$ GeV		Effective mass
Water equiv.	Standard rock		Particles/s	Particles/10 ms	Particles/s	Particles/10 ms	
Surface detector		FLUKA	1700000	17000	1300000	13000	–
$\simeq$ 0.13 km w.e.	50 m	FLUKA	11000	110	10000	100	50 kton
$\simeq$ 0.5 km w.e.	188 m	FLUKA	330	3.3	320	3.2	98 kton
	200 m	GEANT4	–	–	420	4.2	98 kton
$\simeq$ 1 km w.e.	377 m	FLUKA	66	0.66	65	0.65	100 kton
$\simeq$ 2 km w.e.	755 m	FLUKA	6.2	0.062	6.2	0.062	100 kton
$\simeq$ 3 km w.e.	1.13 km	FLUKA	0.96	0.01	0.96	0.01	100 kton
Under the hill (see Figure 8)		GEANT4	–	–	960	9.6	96 kton

TABLE III: Computed average number of muons entering the detector per unit time for various geographical configurations. The effective mass corresponds to the mass of Argon that can be used when, in both 2D readout views, a slice of size 10 cm around each crossing muon is vetoed.

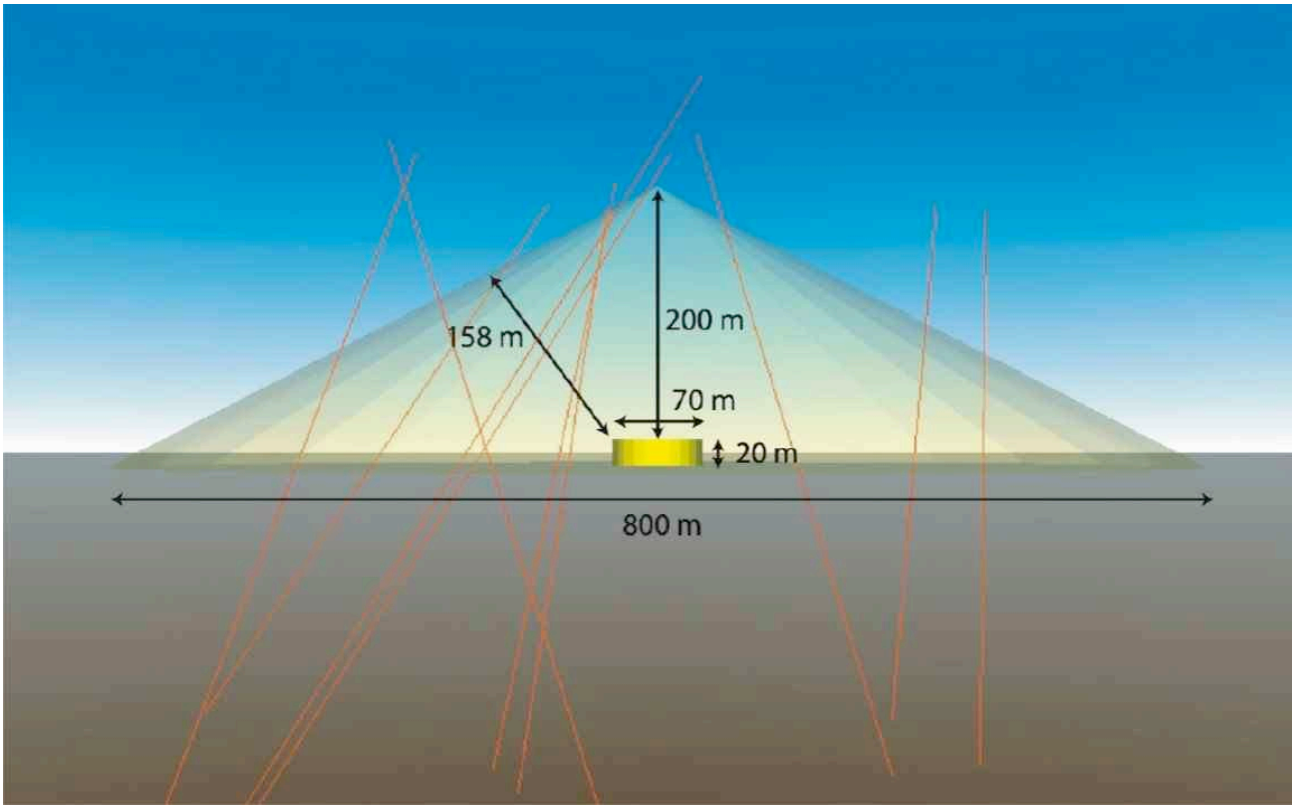

FIG. 8: Under the hill detector configuration. The rock overburden at the vertical of the detector is 200 m and the shortest overburden is 158 m. This geometry has been implemented in a full simulation based on GEANT4.

are shown in Figure 8. The assumed rock overburden at the vertical of the detector is 200 m and the shortest overburden is 158 m. Cosmic ray muons were simulated on a circular area with a radius of 400 m at a height of 200 m above the detector which corresponds to the top of the hill.

The first concern is the average number of muons entering the detector within a time interval of 10 ms, which corresponds to the assumed time for a full drift over 20 m at a field of 1kV/cm [51]. The results are summarized in Table III.

The results from FLUKA and GEANT4 were compared considering a flat Earth surface profile and a detector at $\simeq$ 200 m underground: muon rates agreed within a factor of $\sim$ 1.3. At depths deeper than about 1 km w.e. the rate of crossing muons is less than 1 per 10 ms. Shallower depths e.g. at rock overburdens less than 200 m are disfavored because of detector occupancy (at 50 m rock overburden the average rate of muons with more than 1 GeV crossing in 10 ms is 100). If we assumed that a

slice of size 10 cm in a 2D readout view of the detector around each crossing muon cannot be used for physics, then the rate at resp. 50 m, 188 m would correspond to an available Argon mass of resp. 50 kton, 98 kton. We do not at this stage consider surface operation, as proposed in Ref. [53]. For the under the hill configuration, more than a million muons, corresponding to 156 drifts of 10 ms, were simulated and it was found that on average 9.6 muons enter the Argon volume in 10 ms. This is a factor ~ 2 higher than at an equivalent depth under flat surface, which is still very tolerable.

We now focus on the second step where the rate and energy spectrum of remaining cosmic ray muons at the underground locations is used to study the number of particles entering the detector. We assume that events in which the parent muon enters (before or after the photo-nuclear interaction) the active LAr volume can be discarded thanks a veto based on the liquid Argon imaging. This leads us to restrict the background sources to neutral hadrons and, in particular, to *neutrons*, *neutral kaons* and *lambdas*, produced either directly in muon photo-nuclear interactions or as secondary products in hadronic showers in the materials (e.g. rock) surrounding the detector. We have so far conservatively neglected correlations between neutral hadrons penetrating inside the LAr in conjunction with (visible) charged hadrons.

Neutral hadronic particles have been scored when entering the detector. The energy-integrated number of particles entering the detector per year of exposure at some depths are reported in Table IV. Neutron, neutral kaon and lambda energy spectra on the detector surface are plotted in Figures 9, 10 and 11. Their shapes are practically independent of the depth of rock overburden. Since low energy neutrons are not a background source for nucleon decay searches, we will consider only neutrons with kinetic energy above 20 MeV.

As expected, the particle yields per muons entering the detector, increase with depth, since the average muon energy increases as well. The neutrons yields in the `FLUKA` and `GEANT4` simulations are consistent within a factor of 2. As far as neutral kaons are concerned, there is a difference of a factor of 10. In the case of lambda's, they were not found in the `GEANT4` simulation while in `FLUKA` they are expected at the level of 0.04–0.05 times the rate of neutral kaons. In the following, we will use the yields from `FLUKA` to estimate backgrounds.

In the third phase, neutrons, neutral kaons and lambda's were generated with their expected energy spectrum and were transported in LAr until they underwent an inelastic interaction or decayed. These fully simulated interactions were subjected to the selection cuts and were used to estimate cosmogenic backgrounds (see Section IV C).

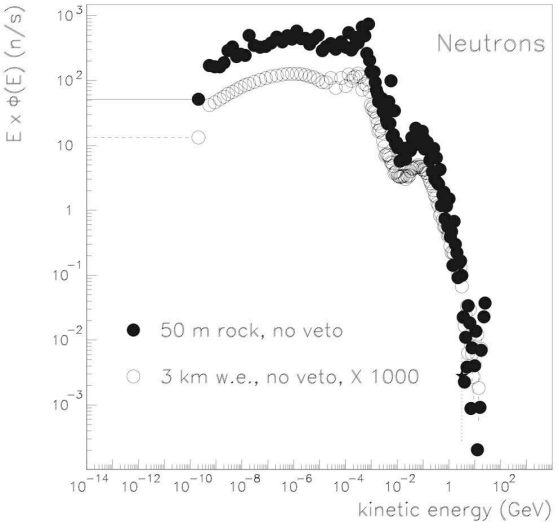

FIG. 9: Energy distribution of neutrons entering the LAr volume as predicted by `FLUKA`.

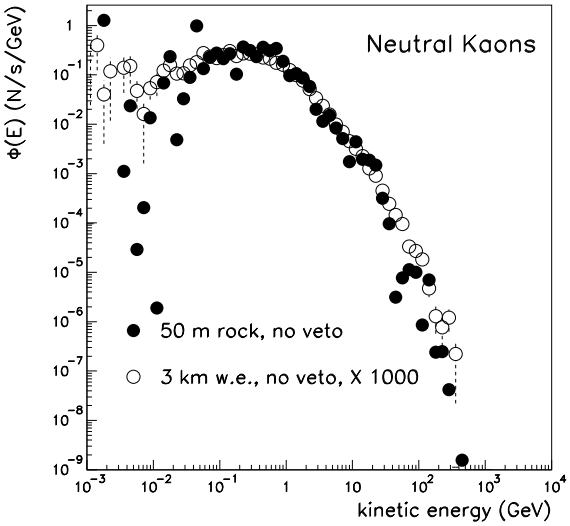

FIG. 10: Energy distribution of neutral kaons entering the LAr volume as predicted by `FLUKA`.

E. An active very large area cosmic muons veto

The spatial distribution of photo-nuclear interactions in a 3 km w.e. depth from which at least one neutron enters the detector is plotted in Figure 12. Most interactions occur along the detector vertical wall, at an av-

Configuration/ Depth	Simulation	Average number μ's entering LAr per 10 ms	Neutrons		Neutral kaons		Lambdas
			per year	per μ in LAr per 10 ms	per year	per μ in LAr per 10 ms	
$\simeq$ 0.5 km w.e. (188 m rock)	FLUKA	3.3	1.9×10^{6}	1.8×10^{-4}	4500	4.3×10^{-7}	$\approx 0.04 \times N_{K^0}$
$\simeq$ 1 km w.e. (377 m rock)	FLUKA	0.66	5.5×10^{5}	2.6×10^{-4}	1300	6.2×10^{-7}	$\approx 0.05 \times N_{K^0}$
$\simeq$ 3 km w.e. (1.13 km rock)	FLUKA	0.01	1.1×10^{4}	3.6×10^{-4}	25	8.2×10^{-7}	$\approx 0.06 \times N_{K^0}$
Under the hill (see Figure 8)	GEANT4 FLUKA rescaled	9.6	9.7×10^{6}	3.2×10^{-4}	1.2×10^{3} $\approx1.2\times10^{4}$	4.0×10^{-8} $\approx4.0\times10^{-7}$	– $\approx 0.05 \times N_{K^0}$

TABLE IV: Cosmogenic background as a function of assumed depth: estimated number of neutrons (with kinetic energy above 20 MeV), neutral kaons and lambda's entering the detector per year, and normalised on the average number of muons entering the active volume per 10 ms, produced in cosmic muon interactions (hadrons accompanied by a detected muon inside LAr imaging have been vetoed).

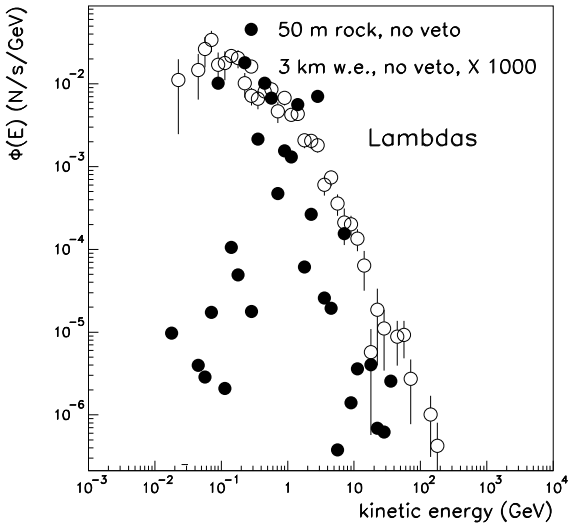

FIG. 11: Energy distribution of lambda particles entering the LAr volume as predicted by FLUKA.

erage distance of one meter from it. The possibility to veto cosmic muon passing in the vicinity of the detector has therefore been investigated.

We considered annular planes of active muon detectors with an inner radius of 35 m and an outer radius of 38 m, to detect muons that pass within 3 m from the LAr active volume (also here we have neglected the details of the liquid Argon tank). Two configurations have been taken into account: (a) two planes at the top and at the bottom of the LAr detector; (b) three planes as shown in Figure 1. In the simulations no assumptions are made regarding their composition, they have a thickness of 1 cm and 100% efficiency for muon crossing the counters. In practice, they could be realized with Resistive Plate Chambers (RPC) [90, 91] or Glass RPCs (GSC) [92]. The total area needed is about 3800 m^2 per plane. In the MONOLITH proposal [93] the total active area was envisaged to be $\approx$ 54000 m^2. Therefore GSC had to be designed in order to allow large-scale production. For techniques on the industrial large area production of glass RPC's see e.g. Ref. [94].

From the simulation in the under the hill configuration, we obtained that about 60% of the muons enter the veto region (i.e. a volume 20 m high and 3 m wide outside the LAr detector) from the top. This value was used as a normalisation to calculate the fraction of muons detected with the two veto configurations, and the results are stated in Table V. Even with the two veto planes configuration, more than 80% of the muons could be detected. In conclusion, an active very large area veto composed of 2 or 3 planes could suppress cosmogenic background by an order of magnitude. In the flat Earth surface geometry or at larger depths, we expect the suppression to be even stronger since muons are more vertically distributed than in the hill configuration. These results will be used in the next section to compute sensitivities to nucleon decays.

IV. NUCLEON DECAY ANALYSIS

The list of studied decay channels in summarized in Table VI.

The approach to discriminate between signal and background is based on a set of sequential selection cuts. Final state topology and event kinematics provide the selection criteria. At first, we ignore the cosmic muon-induced background, and apply cuts until the atmospheric neutrino background can be considered as irreducible.

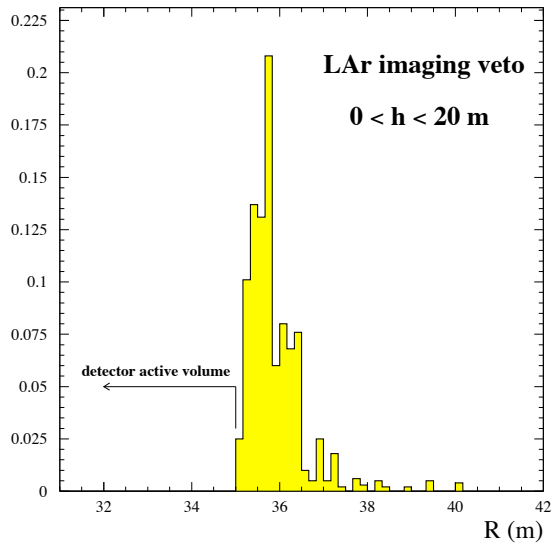

FIG. 12: Radial distribution of photo-nuclear interaction vertexes producing a neutron that enters the detector at a depth of 3 km w.e.

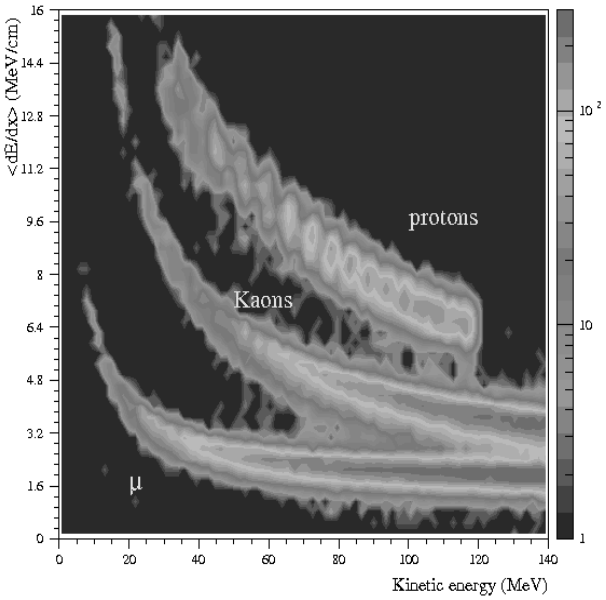

FIG. 13: Scatter plot showing the regions populated by fully simulated muons, kaons and protons on the $< dE/dx >$ vs. kinetic energy plane.

Configuration	Muons ($1.6\times10^6\mu$ simulated per configuration) in 1^{st} veto plane	in veto volume	% detected
Full volume	228	377	100%
3 veto planes	231	361	94%
2 veto planes	243	343	85%

TABLE V: Fraction of muons entering the veto volume and detected using veto planes in different configurations. The veto volume is defined as a cylinder 20 m high and 3 meter wider in radius than the LAr volume.

An efficient background reduction demands a good particle identification. Results based on a dedicated analysis show that the tagging efficiency of pions, kaons and protons is above 99% with contamination below 1%. In addition, the muon–pion misidentification is around 40%. The analysis, based on fully-simulated Monte-Carlo events with single particles, combines several variables in a Multi-layer perceptron Neural Network architecture: the χ^2 fit to the particle hypothesis on the $< dE/dx >$ vs kinetic energy plane, the fitted particle mass and the energy released after the particle decay. Figure 13 shows how, thanks to the fine detector granularity, particles of different species get clearly separated. Electron and photon identification is based on an algorithm that distinguishes single m.i.p. signals versus double m.i.p. signals by using the first hits of each identified electromagnetic track.

The list of selection cuts to reduce the atmospheric neutrino contamination, final efficiencies and background estimations are described in sections IV A and IV B.

We then evaluate the backgrounds due to cosmogenic events. Our strategy is to reduce the contribution from this background at the level of the irreducible atmospheric neutrino background. The amount of cosmogenic background is strongly correlated with the travel path inside the detector. Thus we will cut on the detector fiducial volume, while keeping the same topology and kinematics criteria used for the neutrino-induced background (in this way, signal selection efficiencies are unaltered). The details on the cosmic muon-induced background estimation are given in Section IV C.

A. Proton decay channels

The sequential cuts applied for each channel are briefly described in the following paragraphs. The detailed list of cuts for the considered proton decay channels are listed in Table VII. Survival fraction of signal (first column) and background events from the different atmospheric neutrino interactions after selection cuts are applied in succession are also listed. Backgrounds are normalized to an exposure of 1 Mton×year. The final efficiencies and expected background events after cuts are reported in Table VI. The published efficiencies, backgrounds and results obtained by Super-Kamiokande are shown for comparison.

- $p \rightarrow e^+ \pi^0$ channel: A simulated decay event is shown in Figure 14. The two photons (from the π^0 decay) and the positron flying in the opposite

Decay mode	This paper (LAr TPC) Efficiency (%)	Atmospheric ν background 100 kton×year	Super-Kamiokande results [5, 10] Efficiency (%)	Atmospheric ν background 92 kton×year	Published limit 90% C.L.
(p1) $p \to e^+ \pi^0$	45.3	0.1	40	0.2	1.6×10^{33}
(p2) $p \to \pi^+ \bar{\nu}$	41.9	78.2			
(p3) $p \to K^+ \bar{\nu}$	96.8	0.1	8.6 (prompt-γ)	0.7	2.3×10^{33}
			6.0 ($K^+ \to \pi^+\pi^0$)	0.6	
(p4) $p \to \mu^+ \pi^0$	44.8	0.8	32	0.2	
(p5) $p \to \mu^+ K^0$	46.7	< 0.2	5.4 ($K^0_S \to \pi^0\pi^0$)	0.4	
			7.0 ($K^0_S \to \pi^+\pi^-$ method 1)	3.2	1.3×10^{33}
			2.8 ($K^0_S \to \pi^+\pi^-$ method 2)	0.3	
(p6) $p \to e^+ K^0$	47.0	< 0.2	9.2 ($K^0_S \to \pi^0\pi^0$)	1.1	1.0×10^{33}
			7.9 ($K^0_S \to \pi^+\pi^-$ method 1)	3.6	
			1.3 ($K^0_S \to \pi^+\pi^-$ method 2)	0.04	
(p7) $p \to e^+ \gamma$	98.0	< 0.2	73	0.1	
(p8) $p \to \mu^+ \gamma$	98.0	< 0.2	51	0.2	
(p9) $p \to \mu^- \pi^+ K^+$	97.6	0.1			
(p10) $p \to e^+ \pi^+ \pi^-$	18.6	2.5			
(n1) $n \to \pi^0 \bar{\nu}$	45.1	47.4			
(n2) $n \to e^- K^+$	96.0	< 0.2			
(n3) $n \to e^+ \pi^-$	44.4	0.8			
(n4) $n \to \mu^- \pi^+$	44.8	2.6			

TABLE VI: Summary of studied decay modes: signal detection efficiency and expected atmospheric neutrino background (normalized to 100 kton×year exposure) after selection cuts. Where available, the efficiencies and background results of Super-Kamiokande are given for comparison. The published results obtained by Super-Kamiokande are shown for completeness [5, 10].

direction are clearly visible. In the chosen readout view, the event spreads over about 120×100 cm^2. Figure 15 shows the distributions of the following reconstructed kinematical quantities: the electron momentum, the total momentum imbalance, the invariant mass and the total energy. The distributions are split into the case where the pion leaves the nucleus (full histograms) and the case where it is absorbed (empty histograms). The electron momentum histrogram has an arrow placed at 460 MeV/c, the expected value without Fermi motion and detector effects. It seems clear that two different set of cuts could be implemented to optimize the signal over background ratio in both cases. However, an attempt to look for "inclusive" decays $p \to e^+(\pi^0)$ without condition on the π^0, yields order of magnitudes worse background conditions, and was not considered further.

The list of cuts is presented in Table VII. The idea is to have a balanced event, with all particles identified as such, and with a total visible energy close to the proton mass (see Figure 16). Only one background event for 1 Mton×year exposure survives the cuts, for a signal efficiency of about 45%.

- $p \to \pi^+ \bar{\nu}$ channel: Almost 45% of the events that belong to this channel can not be detected since the π^+ gets absorbed by the nucleus. The cuts are based on the requirement of absence of charged leptons, protons, neutral pions, the presence of one charged pion and a total energy between 350 and 650 MeV. The result is that, for a ∼42% efficiency, the expected background at 1 kton×year exposure is ∼0.8 events.

- $p \to K^+ \bar{\nu}$ channel: this is a quite clean channel due to the presence of a strange meson and no other particle in the final state (see Figure 17). The kaon particle identification is performed and applying the cuts listed in Table VII yields an efficiency ∼97% for a negligible background. The correlation of the reconstructed invariant mass and total momentum is shown in Figure 18.

- $p \to \mu^+ \pi^0$ channel: Almost 53% of the times the π^0 is detected. In this case, cuts are similar to the $e^+\pi^0$ channel. The efficiency remains high (∼45%), while the background is $\simeq$ 8 events for 1 Mton×year.

- $p \to e^+ K^0$ and $p \to \mu^+ K^0$ channels: We concentrate on final states having a K^0_S, since a large fraction of the K^0_L will leave the detector without decaying or will suffer hadronic interactions. In

	Efficiency (%)	**Atmospheric neutrino sources**					
Cuts	**(p1)** $p \to e^+ \pi^0$	ν_e **CC**	$\bar{\nu}_e$ **CC**	ν_μ **CC**	$\bar{\nu}_\mu$ **CC**	ν **NC**	$\bar{\nu}$ **NC**
One π^0	54.0%	6604	2135	15259	5794	8095	3103
One e-shower + no other charged tracks	50.9%	1188	656	1	0	0	0
$p_{tot} < 0.4$ GeV	46.7%	454	127	0	0	0	0
0.86 GeV $< E_{vis} <$ 0.95 GeV	45.3%	1	0	0	0	0	0
Cuts	**(p2)** $p \to \pi^+ \bar{\nu}$	ν_e **CC**	$\bar{\nu}_e$ **CC**	ν_μ **CC**	$\bar{\nu}_\mu$ **CC**	ν **NC**	$\bar{\nu}$ **NC**
No e-shower, no muons, no π^0	92.6%	0	0	34	0	56515	26482
One charged pion	55.7%	0	0	8	0	5632	2027
No protons	50.0%	0	0	4	0	2930	1136
0.35 GeV $<$ Total E $<$ 0.65 GeV	41.9%	0	0	2	0	605	175
Cuts	**(p3)** $p \to K^+ \bar{\nu}$	ν_e **CC**	$\bar{\nu}_e$ **CC**	ν_μ **CC**	$\bar{\nu}_\mu$ **CC**	ν **NC**	$\bar{\nu}$ **NC**
One kaon	96.8%	308	36	871	146	282	77
No other charged tracks, no π^0	96.8%	0	0	0	0	57	9
$E_{vis} < 0.8$ GeV	96.8%	0	0	0	0	1	0
Cuts	**(p4)** $p \to \mu^+ \pi^0$	ν_e **CC**	$\bar{\nu}_e$ **CC**	ν_μ **CC**	$\bar{\nu}_\mu$ **CC**	ν **NC**	$\bar{\nu}$ **NC**
One muon, one π^0	52.8%	0	0	11334	4452	0	0
No protons, no charged pions	50.0%	0	0	1754	1369	0	0
0.86 GeV $<$ Total E $<$ 0.93 GeV	45.3%	0	0	64	41	0	0
Total Momentum < 0.5 GeV	44.8%	0	0	5	3	0	0
Cuts	**(p5)** $p \to \mu^+ K^0_S$	ν_e **CC**	$\bar{\nu}_e$ **CC**	ν_μ **CC**	$\bar{\nu}_\mu$ **CC**	ν **NC**	$\bar{\nu}$ **NC**
One muon + 2 charged or 2 neutral pions	100%	8178	2771	106861	27274	7099	2540
0.4 $<$ Invariant mass of pions $<$ 0.6 GeV	97%	0	0	5	8	6	2
$p_{tot} < 0.6$ GeV	93.4%	0	0	0	0	0	0
Cuts	**(p6)** $p \to e^+ K^0_S$	ν_e **CC**	$\bar{\nu}_e$ **CC**	ν_μ **CC**	$\bar{\nu}_\mu$ **CC**	ν **NC**	$\bar{\nu}$ **NC**
One e-shower + 2 charged or 2 neutral pions	100%	59759	11673	31	0	2	1
0.4 $<$ Invariant mass of pions $<$ 0.6 GeV	97.0%	2	2	0	0	0	0
$p_{tot} < 0.6$ GeV	94.0%	0	0	0	0	0	0
Cuts	**(p7)** $p \to e^+ \gamma$	ν_e **CC**	$\bar{\nu}_e$ **CC**	ν_μ **CC**	$\bar{\nu}_\mu$ **CC**	ν **NC**	$\bar{\nu}$ **NC**
One e-shower + no other charged track	100%	32434	6837	0	0	0	0
Only one photon	99.0%	110	11	0	0	0	0
$p_\gamma > 0.2$ GeV	98.0%	0	0	0	0	0	0
Cuts	**(p8)** $p \to \mu^+ \gamma$	ν_e **CC**	$\bar{\nu}_e$ **CC**	ν_μ **CC**	$\bar{\nu}_\mu$ **CC**	ν **NC**	$\bar{\nu}$ **NC**
One muon + no other charged track	100%	5302	1878	54889	15872	4680	1764
Only one photon	99.0%	7	4	164	13	9	7
$p_\gamma > 0.2$ GeV	98.0%	0	0	0	0	0	0
Cuts	**(p9)** $p \to \mu^- \pi^+ K^+$	ν_e **CC**	$\bar{\nu}_e$ **CC**	ν_μ **CC**	$\bar{\nu}_\mu$ **CC**	ν **NC**	$\bar{\nu}$ **NC**
One Kaon	98.8%	308	36	871	146	282	77
One muon	98.2%	1	0	867	146	0	0
No e-showers	98.2%	0	0	844	145	0	0
0.6 GeV $<$ Total E $<$ 1 GeV	97.6%	0	0	1	0	0	0
Cuts	**(p10)** $p \to e^+ \pi^+ \pi^-$	ν_e **CC**	$\bar{\nu}_e$ **CC**	ν_μ **CC**	$\bar{\nu}_\mu$ **CC**	ν **NC**	$\bar{\nu}$ **NC**
One e-shower, no muons	100%	59755	11673	0	0	0	0
Two charged pions, no protons	19.4%	714	302	0	0	0	0
0.65 GeV $<$ Total E $<$ 1 GeV	19.0%	33	8	0	0	0	0
Total Momentum < 0.57 GeV	18.6%	21	4	0	0	0	0

TABLE VII: Detailed list of cuts for the considered proton decay channels. Survival fraction of signal (first column) and background events through event selections applied in succession. Backgrounds are normalized to an exposure of 1 Mton×year.

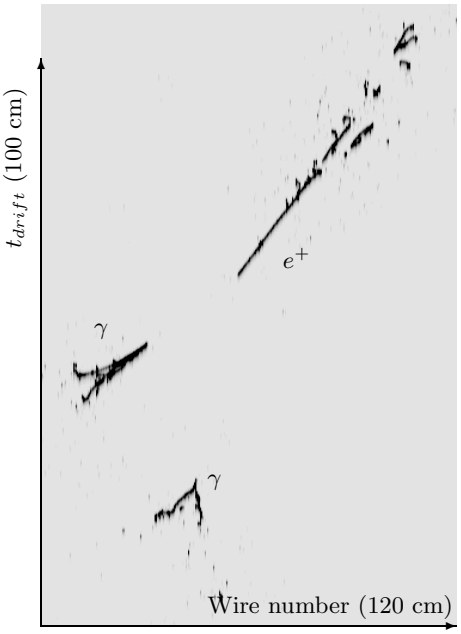

FIG. 14: Simulated $p \rightarrow e^+\pi^0$ event. The displayed area covers 120×100 cm^2.

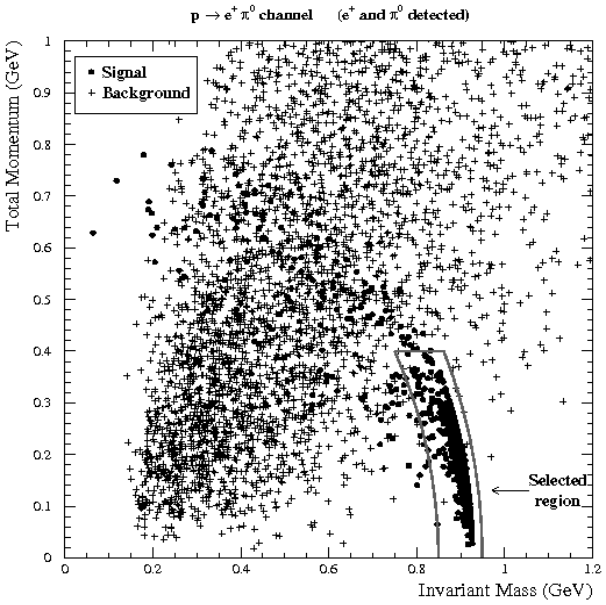

FIG. 16: Kinematic cut in the $p \rightarrow e^+\pi^0$ channel: in the plane defined by the invariant mass and the total momentum, crosses represent background and spots signal events. The band indicates the cut region (0.86 GeV < Total Energy < 0.95 GeV), i.e. all events inside the band are accepted.

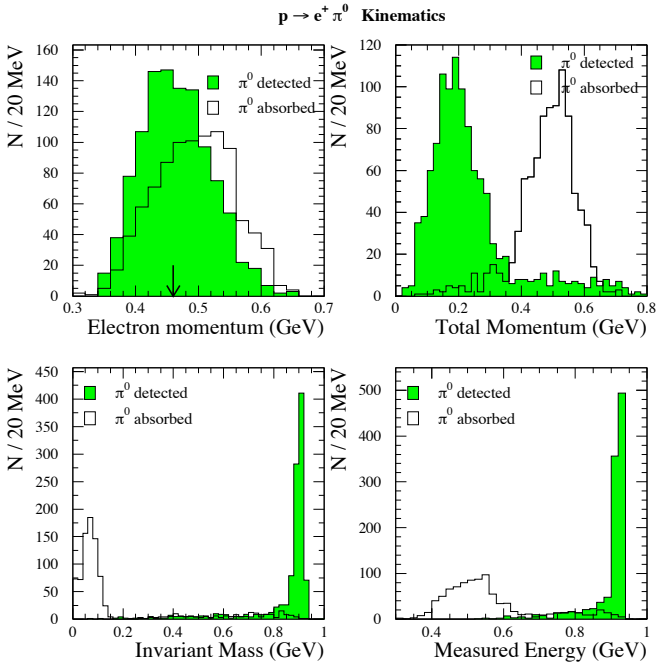

FIG. 15: $p \rightarrow e^+\pi^0$ channel: Distributions of some kinematic variables for the exclusive (full histograms) and the inclusive (empty histograms) scenarios. The arrow in the first plot indicates the value that would have the positron momentum if no Fermi motion and no detector effects were present.

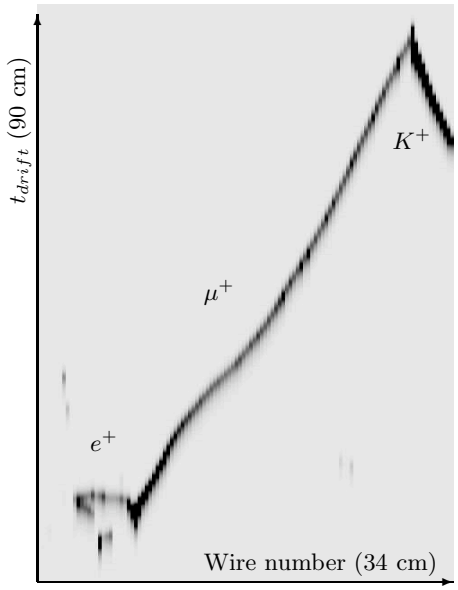

FIG. 17: Simulated $p \rightarrow K^+ \bar{\nu}$ event. The displayed area covers 34×90 cm^2.

Figure 19 simulated events of $p \rightarrow e^+ + K^0_S$ and $p \rightarrow \mu^+ + K^0_S$ decays are shown, where the K^0_S decays into charged pions. A $p \rightarrow \mu^+ + K^0$ decay where K^0 decays into neutral pions is shown in Figure 20. A sophisticated treatment to recover K^0_L events has been neglected at this stage.

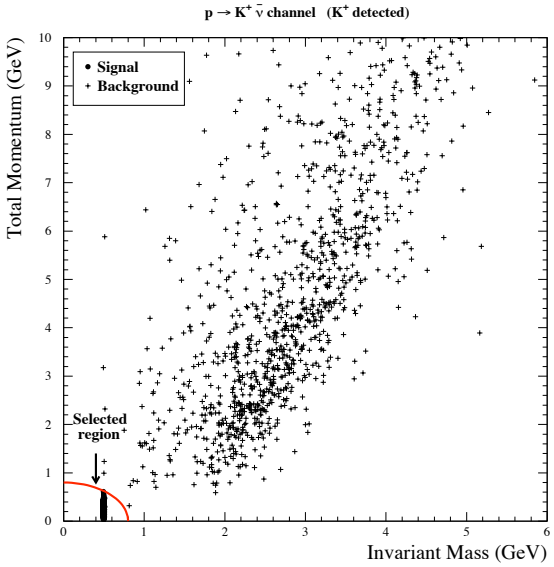

FIG. 18: Kinematic cut in the $p \to K^+\bar{\nu}$ channel: in the plane defined by the invariant mass and the total momentum, crosses represent background and spots signal events. The band indicates the cut region (Total Energy < 0.8 GeV), i.e. all events in the band are accepted.

K^0_S's mainly decay to two pions (either charged or neutral). Simple requirements (an identified lepton in the final state accompanied by two charged (neutral) pions, invariant mass of the pion system consistent with the K^0 mass and total momentum below 0.6 GeV) result in a negligible background contamination for signal selection efficiencies above 90% (see Table VII). The overall efficiency for the $p \to \mu^+(e^+)\, K^0$ channel is therefore 46.7% (47%).

- $p \to e^+\gamma$ and $p \to \mu^+\gamma$ channels: These channels provide a very clean signal thanks to efficient electron and photon separation (see e.g. Ref. [30] for a discussion in the context of e/π^0 separation). The simple final event topology (a single charged lepton accompanied by an energetic photon) allows to reduce the expected background to a negligible level while keeping a signal selection efficiency close to 100% (see Table VII). Simulated events of $p \to e^+ + \gamma$ decay and $p \to \mu^+ + \gamma$ are shown in Figure 21.

- $p \to \mu^-\, \pi^+\, K^+$ channel: by tagging the presence of a K^+ and a μ^-, the background is reduced at the level of ∼1 event for 1 Mton×year exposure. A final cut on the total visible energy removes any background for a signal of ≃ 97%.

- $p \to e^+\, \pi^+\, \pi^-$ channel: The most favorable scenario occurs when the three particles are detected. A tight cut on the total visible energy ($0.65<E_{vis}<1$ GeV) complemented with a cut on the total momentum ($p_{tot}<570$ MeV/c) are sufficient to reduce the contamination of 25 events for a 1 Mton ×year exposure. On the other hand, the cuts remove less than 1% of the signal events.

B. Neutron decay channels

The sequential cuts applied for each channel are briefly described in the following paragraphs. The detailed list of cuts for the considered neutron decay channels are listed in Table VIII. Survival fraction of signal (first column) and background events from the different atmospheric neutrino interactions after selection cuts are applied in succession are also listed. Backgrounds are normalized to an exposure of 1 Mton×year. The final efficiencies and expected background events after cuts are reported in Table VI.

- $n \to \pi^0\, \bar{\nu}$ channel: About ∼45% of the signal events are "invisible" because the π^0 is absorbed in the nucleus. The rest can be disentangled from the background by cutting on the total visible energy and on the total momentum (>0.35 GeV). The final efficiency is ∼45% for ∼0.5 background events at 1 kton×year exposure.

- $n \to e^-\, K^+$ channel: We profit here from the presence of one kaon, one electron and the absence of muons and pions in the final state. These requirements, together with a loose cut on the visible energy ($0.75<E_{vis}<0.95$ GeV), eliminates the background for an almost untouched efficiency.

- $n \to e^+\, \pi^-$ channel: This channel is similar to the $p \to e^+\, \pi^0$ previously reported. When the π^- is detected, a good efficiency can be reached for a negligible background by applying two simple cuts to bound the total energy ($0.75<E_{vis}<1$ GeV) and the positron momentum ($0.35<p_e<0.6$ GeV).

- $n \to \mu^-\, \pi^+$ channel: This channel is treated in a similar way to the $n \to e^+\, \pi^-$. The distribution of the total momentum for signal and background events is shown in Figure 22 and the cuts in Table VIII. We require the presence of a pion on the final state and a cut on the total energy. The plot shows the position of the last cut on total momentum. The final efficiency is ∼45% for the exclusive channel and almost no background events expected.

C. Cosmic muon-induced background estimation

As described in Section III D, the cosmogenic background has been computed in three steps. In the third step, neutrons, neutral kaons and lambda's entering the

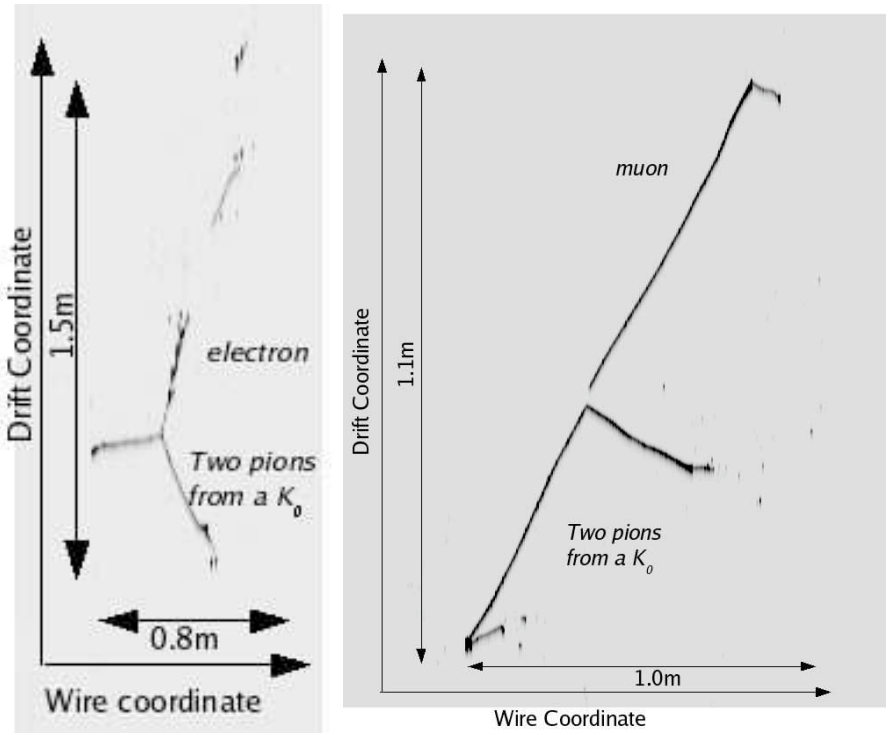

FIG. 19: Simulated $p \to e^+ + K^0$ (left) and $p \to \mu^+ + K^0$ (right) decays. The neutral kaons decay into two charged pions.

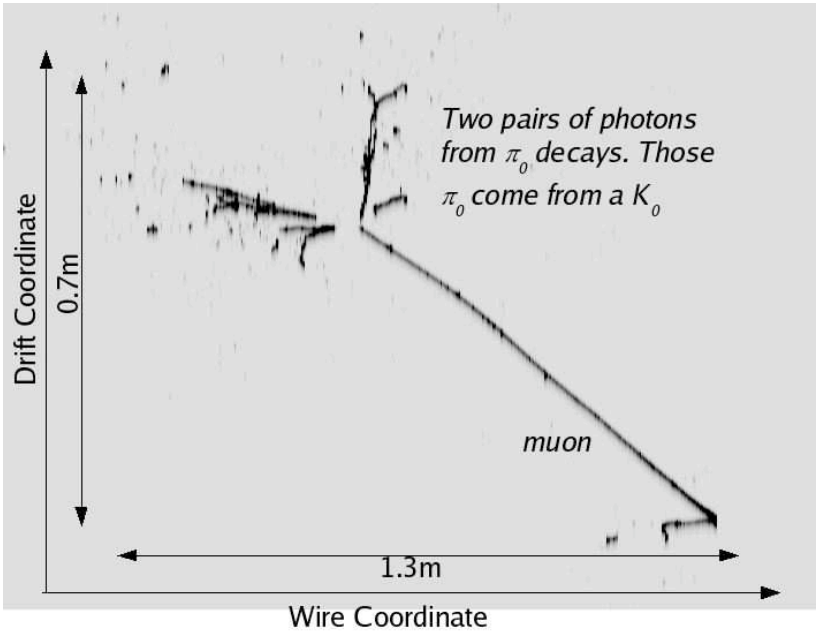

FIG. 20: Simulated $p \to \mu^+ + K^0$ decay. The neutral kaon decays into two neutral pions.

detector were generated according to their expected energy spectrum. We simulated $2{\times}10^5$ events for each particle species and used values in Table IV for normalization. The neutral particles are propagated inside the liquid Argon volume until they interact inelastically or decay. The secondary particles produced in those processes were used in the nucleon decay analysis.

As concrete examples, we discuss in detail the two proton decay channels, $p \to K^+ \, \bar{\nu}$ and $p \to \pi^+ \, \bar{\nu}$, and one neutron decay channel $n \to \pi^0 \, \bar{\nu}$. Other decay chan-

	Efficiency (%)	**Atmospheric neutrino sources**					
Cuts	**(n1)** $n \to \pi^0\ \bar{\nu}$	ν_e **CC**	$\bar{\nu}_e$ **CC**	ν_μ **CC**	$\bar{\nu}_\mu$ **CC**	ν **NC**	$\bar{\nu}$ **NC**
One π^0	56.2%	6604	2135	15259	5794	8095	3103
No muons, no electrons, no charged pions	56.1%	0	0	2	0	4722	1840
No protons	52.6%	0	0	0	0	2964	1184
0.35 GeV < Total E < 0.55 GeV	45.4%	0	0	0	0	469	181
Total Momentum > 0.35 GeV	45.1%	0	0	0	0	362	112
Cuts	**(n2)** $n \to e^-\ K^+$	ν_e **CC**	$\bar{\nu}_e$ **CC**	ν_μ **CC**	$\bar{\nu}_\mu$ **CC**	ν **NC**	$\bar{\nu}$ **NC**
One e-shower, one kaon	97.0%	299	36	11	0	0	0
No π^0 , no muons	97.0%	138	14	0	0	0	0
No charged pions	97.0%	80	5	0	0	0	0
0.75 GeV < Total E < 0.95 GeV	96.0%	0	0	0	0	0	0
Cuts	**(n3)** $n \to e^+\ \pi^-$	ν_e **CC**	$\bar{\nu}_e$ **CC**	ν_μ **CC**	$\bar{\nu}_\mu$ **CC**	ν **NC**	$\bar{\nu}$ **NC**
One e-shower, one charged pion	59.6%	8137	2755	6	0	0	0
No π^0 , no muons, no protons	57.4%	3855	1282	0	0	0	0
0.75 GeV < Total E < 1 GeV	52.4%	499	187	0	0	0	0
0.35 GeV < $P_{positron}$ < 0.6 GeV	51.3%	216	73	0	0	0	0
Total Momentum < 0.35 GeV	44.4%	7	1	0	0	0	0
Cuts	**(n4)** $n \to \mu^-\ \pi^+$	ν_e **CC**	$\bar{\nu}_e$ **CC**	ν_μ **CC**	$\bar{\nu}_\mu$ **CC**	ν **NC**	$\bar{\nu}$ **NC**
One muon, one charged pion	59.4%	1559	454	15931	6569	2291	1055
No π^0, no e-shower, No protons	53.6%	0	0	7830	2924	824	444
0.8 GeV < E_{vis} < 1.05 GeV	49.8%	0	0	1064	408	137	56
p_{tot} < 0.35 GeV	44.8%	0	0	18	2	5	1

TABLE VIII: Detailed list of cuts for the considered neutron decay channels. Survival fraction of signal (first column) and background events through event selections applied in succession. Backgrounds are normalized to an exposure of 1 Mton×year.

nels with a lepton in the final state or more constrained kinematics and topologies, will be less affected by cosmogenic backgrounds. For instance, the probability to misidentify charged pions as muons is at these momenta typically less than 10^{-2}.

In the analysis, we started by applying loose kinematical cuts that rejected cosmogenic events clearly incompatible with nucleon decay signals [95]. For instance, for the channel $p \to \pi^+\ \bar{\nu}$, the expected pion energy in an ideal detector would be 0.48 GeV. We accepted charged pions with energy in the range 0.35–0.65 GeV, since the measured energy is smeared by Fermi motion and detector effects. In the case of strange mesons, we also required an identified kaon in the final state and a total energy below 0.8 GeV. In a second step, same cuts as those defined in Tables VII and VIII were applied to estimate final background contaminations.

Table IX summarizes for each considered channel the remaining muon-induced background level after this selection. The contamination coming from neutrons, kaons and lambdas interactions at different detector depths are shown. We found that the $\pi^\pm$ and π^0 backgrounds are predominantly produced by neutrons, and the $K^\pm$ background is dominated by the K^0_L entering into the detector. For some channels we obtain zero events after the final cut, hence an upper limit for these events occurring in the detector is given. The Λ induced background events appeared to be negligible in comparison to the other sources.

The photo-nuclear interactions, from which at least one neutral particle enters the detector, occur mostly at an average distance of one meter from the detector walls (see Figure 12). Moreover, the number of background events reduces itself essentially exponentially along their path inside the detector due to the self shielding properties of Argon. Therefore, an obvious action to reduce background consists on cutting on the sides of the detector, excluding events produced at a distance smaller than d from the wall (see Figure 23). The fiducial volume is reduced accordingly. The value for the cut distance d for each detector depth can be chosen in such a way that the remaining muon-induced background is of the same order than the irreducible atmospheric neutrino background.

In order to compute the effect of the distance cut on the background events, we consider here the most conservative situation, i.e. the incident neutral background source particles (n and K^0) move horizontally from the top/bottom side wall into the detector (the shortest possible way). After reaching the cut distance d, the particles move along the diagonal of the inner detector cylinder (the longest possible way). We obtain then a simpli-

Depth	Channel	Background source N_b^0 (particles/year)			Cosmogenic background reduction		
		Neutron	K^0	Λ	Distance cut d (m)	Fiducial mass (kton)	Background N_b (events/year)
$\simeq$0.5 km w.e.	$p \to \pi^+\bar{\nu}$	570	–	–	1.5	92	76
(188 m rock)	$n \to \pi^0\bar{\nu}$	450	–	8	1.7	91	46
FLUKA	$p \to K^+\bar{\nu}$	–	135	–	6.6	66	0.1
$\simeq$ 1 km w.e.	$p \to \pi^+\bar{\nu}$	200	–	–	0.7	96	77
(377 m rock)	$n \to \pi^0\bar{\nu}$	130	–	2.3	0.75	96	47
FLUKA	$p \to K^+\bar{\nu}$	–	39	–	5.45	71	0.1
$\simeq$ 3 km w.e.	$p \to \pi^+\bar{\nu}$	4.0	–	–	0	100	4.0
(1.13 km rock)	$n \to \pi^0\bar{\nu}$	2.6	–	–	0	100	2.6
FLUKA	$p \to K^+\bar{\nu}$	–	0.74	–	1.8	90	0.1
Under the hill	$p \to \pi^+\bar{\nu}$	2900	–	–	2.7	85	76
(see Figure 8)	$n \to \pi^0\bar{\nu}$	2300	–	–	2.9	84	46
GEANT4	$p \to K^+\bar{\nu}$	–	36–360	–	5.4–7.5	72–62	0.1
Under the hill	$p \to \pi^+\bar{\nu}$	430	–	–	1.3	93	76
+ two veto planes	$n \to \pi^0\bar{\nu}$	340	–	–	1.5	92	46
GEANT4	$p \to K^+\bar{\nu}$	–	5–54	–	3.65–5.75	80–70	0.1
Under the hill	$p \to \pi^+\bar{\nu}$	170	–	–	0.6	97	77
+ three veto planes	$n \to \pi^0\bar{\nu}$	140	–	–	0.8	95	46
GEANT4	$p \to K^+\bar{\nu}$	–	2–20	–	2.8–5	85–74	0.1

TABLE IX: Cosmogenic background for three selected channels: estimated number of background events per year that survive a kinematic selection. The contamination coming from neutrons, kaons and lambdas interactions at different detector depths are shown. For each detector depth, the radial cut distance and the final fiducial volume to reduce cosmogenic background to the level of the irreducible atmospheric background (resp. 78.2 for $p \to \pi^+\bar{\nu}$, 47.4 for $n \to \pi^0\bar{\nu}$ and 0.1 for $p \to K^+\bar{\nu}$ for an exposure of 100 kton×year) is listed. The range for kaon background is reflecting uncertainty on kaon yields due to differences between FLUKA and GEANT4 results.

fied expression for the normalised background events:

$$N_b = N_b^0 e^{-\frac{d}{c_\lambda}} \frac{R^2}{(R-d)^2} \tag{4}$$

where N_b^0 and N_b are the numbers of events before and after the cut on the fiducial volume, and c_λ is an effective interaction length found to be ~ 71 cm for neutrons and ~ 86 cm for kaons from the MC simulations. With the given number of neutrino produced background events as N_b, the cut distance d can be calculated from the following equation:

$$d = R + 2c_\lambda \mathrm{W}\left(-\frac{R}{2c_\lambda}\sqrt{\frac{N_b^0}{N_b}}e^{-\frac{R}{2c_\lambda}}\right) \tag{5}$$

where the $W(x)$ is the Lambert W-function (or Omega function, inverse of $f(w) = we^w$).

Table IX summarizes, for each considered channel, the distance cuts applied together with the remaining fiducial mass. For each detector depth, the radial cut distance and the final fiducial volume to reduce cosmogenic background to the level of the irreducible atmospheric background (resp. 78.2 for $p \to \pi^+\bar{\nu}$, 47.4 for $n \to \pi^0\bar{\nu}$ and 0.1 for $p \to K^+\bar{\nu}$ for an exposure of 100 kton×year) is listed. The range for kaon background is reflecting uncertainty on kaon yields due to differences between FLUKA and GEANT4 results.

We observe that the background due to charged and neutral pions can be reduced to the same level of expected neutrino-induced backgrounds without a big loss of the detector fiducial mass, even at shallow depth (1 km w.e. or equivalently 380 m of ordinary rock). The rejection of strange mesons requires harder cuts. For a 1 km w.e. depth, a reduction of 30% of the mass is expected. However the prospects for a shallow depth experiment are promising and good sensitivities for most of the analyzed channels are expected for an underground location of 1 km w.e. (see Table X). Similar conclusions hold when a 0.5 km w.e. depth (about 200 m of ordinary rock) is considered. Clearly the situation worsens very much if we consider a position close to surface. For a 50 m rock overburden, the reduction of the pion background requires a reduction by more than 30% of the usable Argon. The reduction of the kaon background implies that half of the available Argon should be used as shield.

Note that using an annular veto system to detect muons as explained in Section III E, the induced background can be reduced by a factor between ~ 5 and ~ 15 (according to the number of planes used), therefore a looser cut on the distance d would be needed and

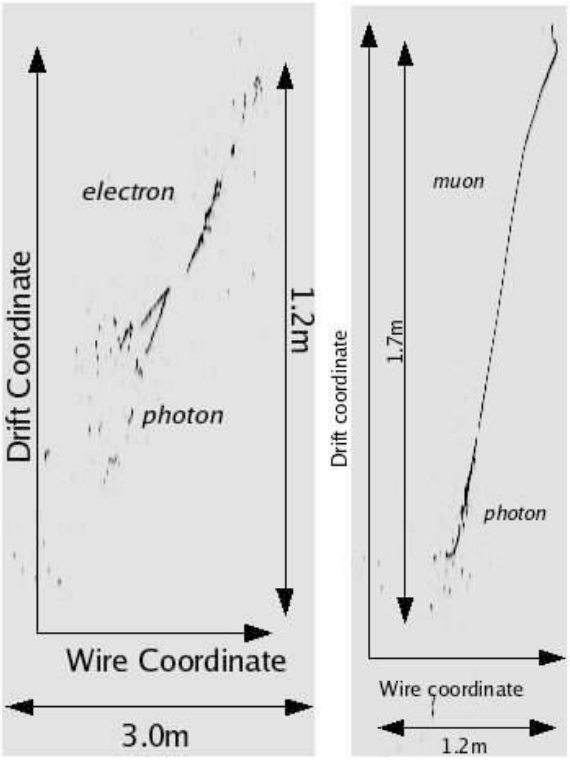

FIG. 21: Simulated $p \to e^+ + \gamma$ and $p \to \mu^+ + \gamma$ decays.

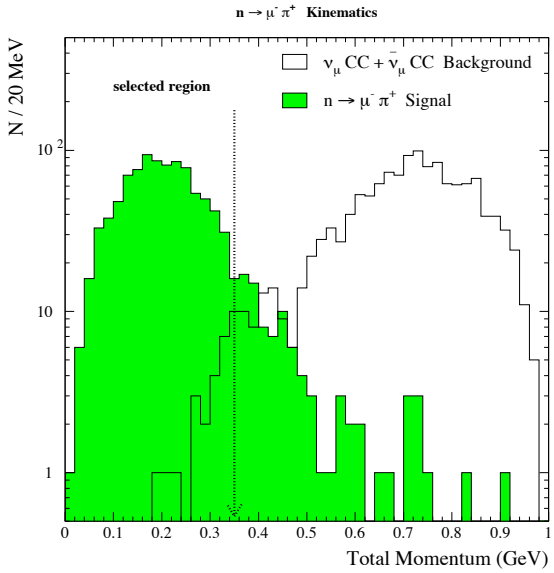

FIG. 22: $n \to \mu^- \pi^+$ channel: distribution of total momentum for events surviving the sixth cut of Table VIII.

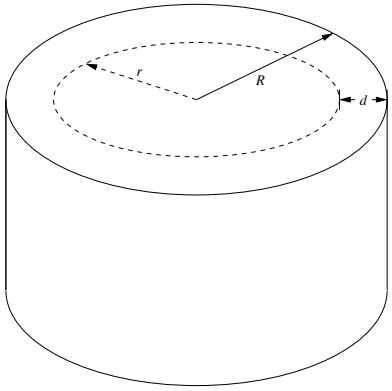

FIG. 23: Schematic view of the radial distance cut to suppress cosmogenic neutral particle background entering the sides of the detector.

it would be possible to have a bigger fiducial volume. For example, the under the hill configuration with three veto planes consents to reduce the distance cut from ≈ 6 m to ≈ 3 m (see Table IX).

V. SENSITIVITY TO NUCLEON DECAY AND COMPARISON TO SUPER-KAMIOKANDE RESULTS

We summarize here the the results from the previous sections for all channels (see Table VI) and compute partial lifetime sensitivities.

In case no signal is observed, limits to proton and neutron partial lifetimes τ/B will be obtained using :

$$(\tau/B)_{proton} > \frac{2.7}{S} \times T \times \epsilon \times 10^{32} \quad \text{(years)} \qquad (6)$$

$$(\tau/B)_{neutron} > \frac{3.3}{S} \times T \times \epsilon \times 10^{32} \quad \text{(years)} \qquad (7)$$

T is the exposure in kilotons $\times$ year, ϵ the signal selection efficiency, and S the constrained 90% CL upper limit on the number of observed signal events, taking into account the fact that there are about 2.7 $\times 10^{32}$ protons and 3.3 $\times 10^{32}$ neutrons in 1 kton of Argon. S is found by solving the equation [85]:

$$\frac{\sum_{n=0}^{n_0} P(n, b+S)}{\sum_{n=0}^{n_0} P(n, b)} = \alpha \qquad (8)$$

$P(n, \mu)$ is the Poisson function, b the estimated background, $\alpha = 0.1$ for a 90% CL, and, n_0 is equal to the closest integer number to b when computing the "detector sensitivity".

For each nucleon decay channel we have computed the (τ/B) limits as a function of the exposure. This is done by rescaling the number of expected background events at each exposure, and computing the corresponding upper limit (S). The result, together with the detection signal efficiency (ϵ), the total expected background and the final detector mass (after fiducial cuts) are reported in Table X. In the channels $p \to \pi^+ \bar{\nu}$, $p \to K^+ \bar{\nu}$, and $n \to \pi^0 \bar{\nu}$, the results at different detector depths are given separately.

The sensitivity of (τ/B) for protons and neutrons as a

Channel	Cut efficiency (%)	Total background per year in fiducial volume	τ/B limit (years) 1 year exposure	τ/B limit (years) 10 years exposure
(p1) $p \to e^+ \pi^0$	45.3	0.1	0.5×10^{34}	0.4×10^{35}
(p2) $p \to \pi^+ \bar{\nu}$	41.9	82 (3 km w.e.)	0.7×10^{33}	0.3×10^{34}
		151 (1 km w.e.)	0.5×10^{33}	0.2×10^{34}
		148 (0.5 km w.e.)	0.5×10^{33}	0.2×10^{34}
		143 (Under the hill)	0.4×10^{33}	0.2×10^{34}
		149 (Under the hill+2 veto planes)	0.5×10^{33}	0.2×10^{34}
		152 (Under the hill+3 veto planes)	0.5×10^{33}	0.2×10^{34}
(p3) $p \to K^+ \bar{\nu}$	96.8	0.2 (3 km w.e.)	1.0×10^{34}	0.6×10^{35}
		0.2 (1 km w.e.)	0.8×10^{34}	0.6×10^{35}
		0.2 (0.5 km w.e.)	0.8×10^{34}	0.4×10^{35}
		0.2 (Under the hill)	(0.8–0.7) $\times 10^{34}$	(0.5–0.4) $\times 10^{35}$
		0.2 (Under the hill+ 2 veto planes)	(0.9–0.8) $\times 10^{34}$	(0.5–0.5) $\times 10^{35}$
		0.2 (Under the hill+ 3 veto planes)	(1.0–0.8) $\times 10^{34}$	(0.6–0.5) $\times 10^{35}$
(p4) $p \to \mu^+ \pi^0$	44.8	0.8	0.4×10^{34}	0.2×10^{35}
(p5) $p \to \mu^+ K^0$	46.7	< 0.2	0.5×10^{34}	0.5×10^{35}
(p6) $p \to e^+ K^0$	47.0	< 0.2	0.5×10^{34}	0.5×10^{35}
(p7) $p \to e^+ \gamma$	98.0	< 0.2	1.1×10^{34}	1.1×10^{35}
(p8) $p \to \mu^+ \gamma$	98.0	< 0.2	1.1×10^{34}	1.1×10^{35}
(p9) $p \to \mu^- \pi^+ K^+$	97.6	0.1	1.1×10^{34}	0.8×10^{35}
(p10) $p \to e^+ \pi^+ \pi^-$	18.6	2.5	0.1×10^{34}	0.5×10^{34}
(n1) $n \to \pi^0 \bar{\nu}$	45.1	50 (3 km w.e.)	0.1×10^{34}	0.5×10^{34}
		92 (1 km w.e.)	0.1×10^{34}	0.4×10^{34}
		89 (0.5 km w.e.)	0.1×10^{34}	0.4×10^{34}
		86 (Under the hill)	0.1×10^{34}	0.3×10^{34}
		90 (Under the hill+ 2 veto planes)	0.1×10^{34}	0.4×10^{34}
		91 (Under the hill+ 3 veto planes)	0.1×10^{34}	0.4×10^{34}
(n2) $n \to e^- K^+$	96.0	< 0.2	1.4×10^{34}	1.4×10^{35}
(n3) $n \to e^+ \pi^-$	44.4	0.8	0.4×10^{34}	0.2×10^{35}
(n4) $n \to \mu^- \pi^+$	44.8	2.6	0.4×10^{34}	0.2×10^{35}

TABLE X: Summary table of the main nucleon decay search results. For each channel, the signal detection efficiency and the total expected background are given together with the lifetime limit at 90% CL for 1 and 10 years of data-taking. For the $p \to K^+\bar{\nu}$ the range reflects the difference of yields of kaons per muon from `FLUKA` and `GEANT4`.

function of the exposure is illustrated in Figure 24 considering only atmospheric neutrino background (left) and including the cosmogenic background (right). In the latter case the plot is shown as a function of exposure in years since there is a reduction in fiducial mass taken into account to reduce the background according to Table IX, while the sensitivity curves without cosmogenic background are plotted as a function of the exposure in kton $\times$ year.

The liquid Argon TPC, offering good granularity and energy resolution, low particle detection threshold, and excellent background discrimination, can yield good signal over background ratios in many possible decay modes, allowing to reach partial lifetime sensitivities in the range of $10^{34} - 10^{35}$ years often in background free conditions up to exposures of 1000 kton$\times$year. This situation is optimal for discoveries at the few-events level. In particular:

- Multi-prong decay modes like e.g. $p \to \mu^-\pi^+K^+$ or $p \to e^+\pi^+\pi^-$ and channels involving kaons like e.g. $p \to K^+\bar{\nu}$, $p \to e^+K^0$ and $p \to \mu^+K^0$ are particularly suitable, since liquid Argon imaging provides typically an order of magnitude improvement in efficiencies for similar or better background conditions compared to Super-Kamiokande results.

- Up to a factor 2 improvement in efficiency is expected for modes like $p \to e^+\gamma$ and $p \to \mu^+\gamma$ thanks to the clean photon identification and separation from π^0.

- Channels like $p \to e^+\pi^0$ or $p \to \mu^+\pi^0$, dominated by intrinsic nuclear effects, yield similar efficiencies and backgrounds as in Super-Kamiokande.

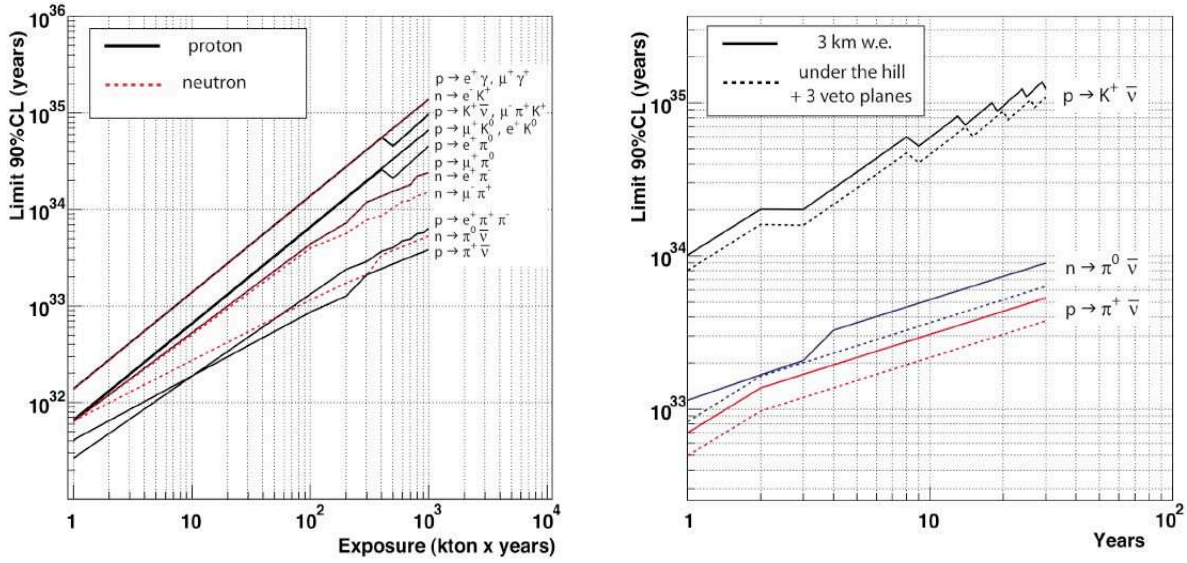

FIG. 24: Running of the nucleon partial lifetime sensitivity (τ/B at 90% C.L.) as a function of exposure (left) considering only atmospheric neutrino background (right) with cosmogenic background and corresponding reduction in fiducial mass taken into account (see text).

Thanks to the self-shielding and 3D-imaging properties of the liquid Argon TPC, these results remains valid even at shallow depths where cosmogenic background sources are important. A very large area annular active muon veto shield could be used in order to further suppress cosmogenic backgrounds at shallow depths. For example, our results show that a three plane active veto at a shallow depth of about 200 m rock overburden in the under the hill configuration yields similar sensitivity for $p \to K^+\bar{\nu}$ as a 3 km w.e. deep detector.

VI. CONCLUSIONS

The most direct sign for Grand Unification is the experimental detection of proton or bound-neutron decays. In order to reach partial lifetime in the relevant range, new generation massive underground detectors with fine tracking and excellent calorimetry are needed to suppress backgrounds with a good signal selection efficiency. Furthermore, the detector should be sensitive to several different channels in order to better understand the nucleon decay mechanism.

In this paper we have estimated the discovery potential of liquid Argon TPC detectors and compared it to the existing results of Super-Kamiokande. We have analyzed many possible neutron and proton decay channels and for the first time the two sources of background contamination: atmospheric neutrinos and cosmogenic backgrounds.

Our results indicate that a liquid Argon TPC, if scaled at the relevant mass scale of the order of 100 kton, offering good granularity and energy resolution, low particle detection threshold, and excellent background discrimination, can yield good signal over background ratios in many possible decay modes, allowing to reach partial lifetime sensitivities in the range of $10^{34} - 10^{35}$ years with exposures up to 1000 kton×year, often in quasi-background-free conditions optimal for discoveries at the few events level, corresponding to atmospheric neutrino background rejections of the order of 10^5.

Multi-prong decay modes like e.g. $p \to \mu^-\pi^+K^+$ or $p \to e^+\pi^+\pi^-$ and channels involving kaons like e.g. $p \to K^+\bar{\nu}$, $p \to e^+K^0$ and $p \to \mu^+K^0$ are particularly suitable, since liquid Argon imaging provides typically an order of magnitude improvement in efficiencies for similar or better background conditions compared to Super-Kamiokande.

Up to a factor 2 improvement in efficiency is expected for modes like $p \to e^+\gamma$ and $p \to \mu^+\gamma$ thanks to the clean photon identification and separation from π^0.

Channels like $p \to e^+\pi^0$ or $p \to \mu^+\pi^0$, dominated by intrinsic nuclear effects, yield similar efficiencies and backgrounds as in Super-Kamiokande.

Thanks to the self-shielding and 3-D imaging properties of the liquid Argon TPC, this result remains valid even at shallow depths where cosmogenic background sources are important. We consider the possibility of a very large area annular active muon veto shield in order to further suppress cosmogenic backgrounds at shallow depths.

In conclusion, we find that this class of detectors does not necessarily require very deep underground laboratories, like those typically encountered in existing or planned sites, to perform very sensitive nucleon decay searches. As a concrete example, we considered a three-

plane annular active veto surrounding a detector at a shallow depth of about 200 m rock overburden in an under the hill configuration and found that it yields similar sensitivities, in particular for $p \to K^+\bar{\nu}$, as for a 3 km w.e. deep detector.

In addition to a successful completion of the required technological R&D necessary to reach the relevant mass scale of 100 kton in a cost-effective way, we point out the importance of an experimental verification of the liquid Argon TPC physics potentialities to detect, reconstruct and classify events in the relevant energy range. This experimental verification will require in addition to possible specific tests in charged particle beams, the collection and study of neutrino events in GeV range with statistics of the order of 100'000 events or more.

VII. ACKNOWLEDGMENTS

This work was in part supported by ETH and the Swiss National Foundation. AB, AJM and SN have been supported by CICYT Grants FPA-2002-01835 and FPA-2005-07605-C02-01. SN acknowledges support from the Ramon y Cajal Programme. We thank P. Sala for help with `FLUKA` while she was an ETH employee. We thank A. Marchionni for a careful reading of the manuscript.

[1] J. Pati and A. Salam, Phys. Rev. D8, 1240 (1973).
[2] H. Georgi and S. L. Glashow, Phys. Rev. Lett. **32**, 438 (1974).
[3] U. Amaldi, W. de Boer and H. Furstenau, Phys. Lett. B **260**, 447 (1991).
[4] P. Langacker, Phys. Rept. **72**, 185 (1981).
[5] M. Shiozawa *et al.* [Super-Kamiokande Collaboration], Phys. Rev. Lett. **81**, 3319 (1998) [arXiv:hep-ex/9806014].
[6] M. Shiozawa [Super-Kamiokande Collaboration], *Prepared for 28th International Cosmic Ray Conferences (ICRC 2003), Tsukuba, Japan, 31 Jul - 7 Aug 2003*
[7] J.Wess and B.Zumino, Nucl. Phys. **B70**, 39 (1974).
[8] K.S. Babu, J.C. Pati and F. Wilczek, Nucl. Phys. B566, 33 (2000).
[9] Y. Hayato *et al.* [Super-Kamiokande Collaboration], Phys. Rev. Lett. **83**, 1529 (1999) [arXiv:hep-ex/9904020].
[10] K. Kobayashi *et al.* [Super-Kamiokande Collaboration], Phys. Rev. D **72**, 052007 (2005) [arXiv:hep-ex/0502026].
[11] S. Dimopoulos and H. Georgi, Nucl. Phys. B **193**, 150 (1981).
[12] N. Sakai and T. Yanagida, Nucl. Phys. **B197**, 533 (1982).
[13] J. Hisano, H. Murayama, and T. Yanagida, Nucl. Phys. **B402**, 46 (1993), hep-ph/9207279.
[14] P. Nath, A. H. Chamseddine, and R. Arnowitt, Phys. Rev. **D32**, 2348 (1985).
[15] P. Nath and R. Arnowitt, (1998), hep-ph/9808465.
[16] Q. Shafi and Z. Tavartkiladze, Phys. Lett. **B473**, 272 (2000), hep-ph/9911264.
[17] V. Lucas and S. Raby, Phys. Rev. **D55**, 6986 (1997), hep-ph/9610293.
[18] J. C. Pati, Int. J. Mod. Phys. **A18**, 4135 (2003), hep-ph/0305221.
[19] K. S. Babu, J. C. Pati, and F. Wilczek, Phys. Lett. **B423**, 337 (1998), hep-ph/9712307.
[20] K. S. Babu, J. C. Pati, and F. Wilczek, Nucl. Phys. **B566**, 33 (2000), hep-ph/9812538.
[21] J. C. Pati, (2000), hep-ph/0005095.
[22] J. R. Ellis, D. V. Nanopoulos, and J. Walker, Phys. Lett. **B550**, 99 (2002), hep-ph/0205336.
[23] N. Arkani-Hamed, S. Dimopoulos, G. F. Giudice and A. Romanino, Nucl. Phys. B **709**, 3 (2005) [arXiv:hep-ph/0409232].
[24] A. Hebecker and J. March-Russell, Phys. Lett. **B539**, 119 (2002), hep-ph/0204037.
[25] M. L. Alciati, F. Feruglio, Y. Lin, and A. Varagnolo, JHEP **03**, 054 (2005), hep-ph/0501086.
[26] I. R. Klebanov and E. Witten, Nucl. Phys. **B664**, 3 (2003), hep-th/0304079.
[27] P. Nath and P. F. Perez, arXiv:hep-ph/0601023.
[28] S. Wiesenfeldt, arXiv:hep-ph/0610273.
[29] A. Rubbia, arXiv:hep-ph/0407297.
[30] A. Meregaglia and A. Rubbia, JHEP **0611**, 032 (2006) [arXiv:hep-ph/0609106].
[31] A. Rubbia, "LAGUNA - Large Apparatus for Grand Unified and Neutrino Astrophysics", Invited talk at the 8^{th} international workshop on Neutrino Factories, Superbeams and Betabeams NUFACT06, August 2006, Irvine (USA).
[32] K. Nakamura, Front. Phys. **35**, 359 (2000).
[33] Y. Suzuki *et al.* [TITAND Working Group], arXiv:hep-ex/0110005.
[34] C. K. Jung, AIP Conf. Proc. **533**, 29 (2000) [arXiv:hep-ex/0005046].
[35] M. V. Diwan and C. K. Jung, *Prepared for International Workshop on Next Generation Nucleon Decay and Neutrino Detector (NNN 99), Stony Brook, New York, 23-25 Sep 1999*
[36] A. de Bellefon *et al.*, arXiv:hep-ex/0607026.
[37] T. Marrodan Undagoitia, F. von Feilitzsch, M. Goger-Neff, K. A. Hochmuth, L. Oberauer, W. Potzel and M. Wurm, Prog. Part. Nucl. Phys. **57**, 290 (2006).
[38] T. Marrodan Undagoitia *et al.*, J. Phys. Conf. Ser. **39**, 269 (2006).
[39] C. Rubbia, CERN-EP/77-08 (1977).
[40] E. Aprile, K. L. Giboni and C. Rubbia, Nucl. Instrum. Meth. A **241**, 62 (1985).
[41] P. Benetti *et al.*, Nucl. Instrum. Meth. A 332 (1993) 395.
[42] P. Cennini *et al.*, Nucl. Instrum. Meth. A 345 (1994) 230.
[43] F. Arneodo *et al.* [ICARUS-Milano Collaboration], Phys. Rev. D 74, 112001 (2006) [arXiv:physics/0609205].
[44] S. Amerio *et al.*, Nucl. Instrum. Meth. A 527 (2004) 329 and references therein.
[45] S. Amoruso *et al.*, Nucl. Instrum. Meth. A **516** (2004) 68.
[46] S. Amoruso *et al.* [ICARUS Collaboration], Nucl. Instrum. Meth. A **523**, 275 (2004).
[47] A. Badertscher, M. Laffranchi, A. Meregaglia and A. Rubbia, New J. Phys. **7**, 63 (2005)

[arXiv:physics/0412080].
[48] A. Badertscher, M. Laffranchi, A. Meregaglia, A. Muller and A. Rubbia, Nucl. Instrum. Meth. A **555**, 294 (2005) [arXiv:physics/0505151].
[49] A. Bueno, M. Campanelli, A. Ferrari and A. Rubbia, AIP Conf. Proc. **533** (2000) 12.
[50] W. Haxton, "Underground laboratories", Invited talk at the 8^{th} international workshop on Neutrino Factories, Superbeams and Betabeams NUFACT06, August 2006, Irvine (USA).
[51] A. Rubbia, arXiv:hep-ph/0402110.
[52] D. B. Cline, F. Raffaelli and F. Sergiampietri, JINST **1** (2006) T09001 [arXiv:astro-ph/0604548]. D. B. Cline, F. Sergiampietri, J. G. Learned and K. McDonald, Nucl. Instrum. Meth. A **503**, 136 (2003) [arXiv:astro-ph/0105442].
[53] L. Bartoszek *et al.*, arXiv:hep-ex/0408121.
[54] A. Ereditato and A. Rubbia, Nucl. Phys. Proc. Suppl. **155**, 233 (2006) [arXiv:hep-ph/0510131].
[55] A. Ereditato and A. Rubbia, Nucl. Phys. Proc. Suppl. **154**, 163 (2006) [arXiv:hep-ph/0509022].
[56] A. Rubbia, Talk given at the ISS meeting held on July 3rd, 2006.
[57] E. Kearns *et al.*, "A Proposal for a Detector 2 km Away From the T2K Neutrino Source", document submitted to DOE NuSAG, May 2005.
[58] T H Dey and T J Lewis, Brit. J. Appl. Phys., Ser 2, 1 (8), 1968, 10191029.
[59] P. Nemethy, P. J. Oddone, N. Toge and A. Ishibashi, Nucl. Instrum. Meth. **212**, 273 (1983).
[60] S. R. Amendolia *et al.*, Nucl. Instrum. Meth. A **239** (1985) 192.
[61] L. Kaufmann and A. Rubbia, arXiv:hep-ph/0611288.
[62] L. Bruschi, B. Maraviglia, and F.E. Moss, Phys. Rev. Lett. 17 (1966), 682.
[63] G.W. Rayfield and W. Schoepe, Phys. Lett. A34 (1971) 133.
[64] L. Bruschi, G. Mazzi, M. Santini, and G. Torzo, J. Phys. C: Solid State Phys., Vol. 8 (1975), 1412 .
[65] A.F. Borghesani, G. Carugno, M. Cavenago, and E. Conti, Phys. Lett. A149 (1990), 481 .
[66] W. Tauchert, H. Jungblut, W.F. Schmidt, Can. J. Chem., v.55, n.11 (1977) 1860.
[67] A J Walters, J. Phys. D: Appl. Phys. 36 2743-2749.
[68] K. Shinsaka, M. Codama, T. Srithanratana, M. Yamamoto, Y. Hatano, J. Chem. Phys., vol.88, pp. 7529–7536, 1988.
[69] J. Allison *et al.*, IEEE Trans. Nucl. Sci. **53** (2006) 270.
[70] S. Agostinelli *et al.* [GEANT4 Collaboration], Nucl. Instrum. Meth. A **506**, 250 (2003).
[71] P. Cennini *et al.*, Nucl. Instrum. Meth. A **432**, 240 (1999).
[72] A. Ferrari, P. R. Sala, A. Fasso and J. Ranft, CERN-2005-10 (2005), INFN/TC-05/11, SLAC-R-773 and references therein.
[73] G. Battistoni, P. R. Sala and A. Ferrari, Acta Phys. Polon. B **37**, 2361 (2006).
[74] G. Battistoni, A. Ferrari, T. Montaruli and P. R. Sala, Astropart. Phys. **19**, 269 (2003) [Erratum-ibid. **19**, 291 (2003)] [arXiv:hep-ph/0207035].
[75] M. Honda, T. Kajita, K. Kasahara and S. Midorikawa, Phys. Rev. D **70**, 043008 (2004) [arXiv:astro-ph/0404457].
[76] A. Rubbia, talk at the First International Workshop on Neutrino-Nucleus Interactions in the Few GeV Region (Nuint 01), December 2001, KEK, Tsukuba, Japan.
[77] J. Altegoer *et al.* [NOMAD Coll.], Nucl. Instrum. Meth. A404, 96 (1998).
[78] D. Casper, Nucl. Phys. Proc. Suppl. **112**, 161 (2002) [arXiv:hep-ph/0208030].
[79] D. Kielcewska and P. Przewlocki, private communication.
[80] P. Astier *et al.* [NOMAD Collaboration], Nucl. Phys. B **621**, 3 (2002) [arXiv:hep-ex/0111057].
[81] T. Sjostrand and M. Bengtsson, Comput. Phys. Commun. **43**, 367 (1987).
[82] Y. Ge, PhD Thesis, No. 16894, ETH Zürich, Switzerland (2006) [unpublished]. Available at *http://neutrino.ethz.ch*.
[83] G. Battistoni, A. Ferrari, C. Rubbia, P. R. Sala and F. Vissani, arXiv:hep-ph/0604182.
[84] M. Crouch, in Proc. of the 20th International Cosmic Ray Conference (ICRC), Vol.6, p.165 (1987).
[85] W. M. Yao *et al.* [Particle Data Group], J. Phys. G **33**, 1 (2006).
[86] M. Ambrosio *et al.* [MACRO Collaboration.], Phys. Rev. D **52**, 3793 (1995).
[87] V.A. Kudryavtsev *et al.*, Nucl. Instr. Meth. A505, 688 (2003).
[88] L.B. Bezrukov and E.V. Bugaev, Yad. Fiz. 33, 1195 (1981).
[89] Y.F. Wang *al.*, Phys. Rev. D 64, 013012 (2001).
[90] R. Santonico and R. Cardarelli, Nucl. Instrum. Meth. **187**, 377 (1981).
[91] R. Bellazzini, C. Betti, A. Brez, E. Carboni, M. M. Massai and M. R. Torquati, Nucl. Instrum. Meth. A **247**, 445 (1986).
[92] C. Gustavino *et al.*, Nucl. Instrum. Meth. A **315** (1992) 507.
[93] MONOLITH Collaboration, "A Massive Magnetized Iron Detector for Neutrino Oscillation Studies, Experiment Proposal, LNGS P26/2000,CERN/SPSC 2000-031,SPSC/M657, August 15th, 2000.
[94] G. C. Trinchero, A. Giuliano and P. Picchi, Nucl. Instrum. Meth. A **508**, 102 (2003).
[95] Z. Dai, PhD Thesis, No. 16133, ETH Zürich, Switzerland (2005) [unpublished]. Available at *http://neutrino.ethz.ch*.
[96] The scintillation light signal has not being used in the present analysis, but will in the case of the actual experiment yield the T_0 of the event, allowing to reconstruct the position of the event along the drift direction.
[97] The DIS process includes single-pion production via baryon resonance excitation within a parton model formalism, inspired from the concept of duality.
[98] If the rock is well known and of very good quality in a given site, a new hole in virgin ground can be considered. See [31] and references therein.
[99] The geography of the chosen location was estimated with the Google Earth tool. See `http://earth.google.com`.